nature communications

Article

https://doi.org/10.1038/s41467-025-67133-5

Activation of hypothalamic-pontine-spinal pathway promotes locomotor initiation and functional recovery after spinal cord injury in mice

Received: 4 March 2025

Accepted: 23 November 2025

Published online: 06 December 2025

Check for updates

Chengyue Ji[1,2,7], Yunfan Zhang[2,3,7], Zeyu Lin[2,7], Ziqi Zhao[2,3], Zhuolei Jiao[2], Zhiyuan Zheng[4], Xiaoxue Shi[2], Xiaofei Wang[2], Ziyu Li[2,5], Shuisheng Yu[2,5], Yun Qu[2,3], Yaxuan Wei[2,3], Tan Rui[2], Bowen Zheng[2], Taorong Xie[2], Hanyu Shi[2], Qifang Wang[2], Xiao Yu[2], Xiaohong Xu[2], Juxiang Chen[4], Jin Fan[1], Weihua Cai[1] ✉ & Yi Li[2,3,6] ✉

The hypothalamus is critical for regulating behaviors essential for survival and locomotion, but how it integrates internal needs and transmits locomotion commands to the spinal cord (SC) remains unclear. We found that glutamatergic neurons in lateral hypothalamic area (LHA) are essential for regulating motivated locomotor activity. Using single-neuron projectome analysis, transsynaptic tracing, and optogenetic manipulation, we showed that LHA facilitates motivated locomotion during food seeking via pontine reticular nucleus, oral part (PnO) projection neurons, rather than direct SC projections or indirect stress signaling via medial septum and diagonal band. Activating PnO-SC projection neurons also initiated locomotion. Importantly, LHA-PnO projection neurons were crucial for regulating locomotor recovery following mouse spinal cord injury (SCI). Motor cortex signals gated LHA deep brain stimulation treatment markedly promoted long-term restoration of hindlimb motor functions after severe SCI. Thus, we have identified a hypothalamic-pontine-spinal pathway and the stimulation paradigm for potential therapeutic intervention after SCI.

Locomotion is a fundamental behavior that is essential for survival, as it enables animals to seek food, evade threats, and engage in social and reproductive activities. Two primary command centers in the brain, the subthalamic locomotor region (SLR) and the mesencephalic locomotor region (MLR), are responsible for transmitting locomotor commands to the central pattern generators in the spinal cord[1–4]. Extensive studies have revealed the role of the MLR in controlling locomotion speed and various aspects of body movement[5–8], but the mechanisms by which the SLR integrates internal/external stimulation and transmits locomotor commands to the spinal cord remain unclear.

The lateral hypothalamic area (LHA) within the SLR has been implicated in motor control, particularly in motivated locomotion—internal need-driven movements such as food-seeking, exploration, or goal-directed behaviors[9,10]. However, the precise LHA circuits that

[1]Department of Orthopedics, The First Affiliated Hospital of Nanjing Medical University, Nanjing, Jiangsu, China. [2]Institute of Neuroscience, Center for Excellence in Brain Science and Intelligence Technology, Chinese Academy of Sciences, Shanghai, China. [3]University of Chinese Academy of Sciences, Beijing, China. [4]Department of Neurosurgery, Shanghai Changhai Hospital Naval Medical University, Shanghai, China. [5]Department of Orthopedics, The Second Affiliated Hospital of Anhui Medical University, Hefei, Anhui, China. [6]China-Hungary Belt-and-Road joint Laboratory on Brain Science, Shanghai, China. [7]These authors contributed equally: Chengyue Ji, Yunfan Zhang, Zeyu Lin. ✉e-mail: caiwhspine@sina.com; liyi@ion.ac.cn

control locomotion, particularly in the context of motivation, remain incompletely understood[3,11]. Recent single-neuron projectome studies have begun to reveal more detailed connections between specific neuronal subtypes in distinct brain regions, and these studies have provided insights into how these circuits may coordinate complex behaviors[12–16].

Defining the neural circuits that control locomotion is also crucial for developing neural circuit-based strategies to promote motor recovery following injuries of the central nervous system (CNS). This is particularly relevant in the case of SCI, in which the brain loses its direct connection with the SC. Despite the neuronal death and axon degeneration that occur after SCI, some axons and dormant relay pathways often remain spared across the lesion site, providing a neural substrate that can be reactivated to promote functional recovery, even with limited axon regeneration[17]. Moreover, the restoration of locomotor function after SCI involves the reorganization of both spinal and supraspinal circuits[18]. Recent studies have revealed the contributions of specific brain regions to the recovery of motor function after SCI, further suggesting the importance of reactivating the neural circuits that are involved in regulating locomotion control[19–22]. However, effective therapeutic strategies for restoring motor function after SCI remain limited. As a promising strategy for in vivo neuronal activation, deep brain stimulation (DBS) offers the advantage of locally activating specific brain nuclei. Notably, Masini et al. successfully employed this approach to rescue motor deficits through the targeted manipulation of PPN glutamatergic neurons in a Parkinsonian mouse model[23]. Additionally, recent studies have revealed that targeting specific MLR regions, including cuneiform nucleus (CnF)[24–26] and pedunculopontine nucleus (PPN)[27], can enhance motor function and promote recovery in animal SCI models. However, the precise brain nuclei that should be targeted to achieve optimal motor recovery remain under investigation[28], and clinical trials are still in their early stages[29,30].

Here, we employed a range of advanced techniques, including whole-brain trans-synaptic labeling, single-neuron projectome analysis, and projection-specific targeting, to investigate the contributions of the hypothalamic LHA nucleus in locomotion control and in motor function restoration following SCI. Our findings suggest that LHA facilitates motivated locomotion through an indirect pathway, particularly the pontine reticulospinal tract, rather than through direct projections to the spinal cord or through connections to the medial septum and diagonal band (MSDB). This indirect modulation of spinal circuits offers a target for therapeutic intervention. Moreover, we investigated the potential of DBS targeting the LHA to promote motor recovery, with the ultimate goal of developing a translatable strategy for restoring locomotion in individuals with severe SCI.

Results

LHA glutamatergic neurons are involved in hindlimb motor control

To visualize the hypothalamic areas that directly or indirectly project to the hindlimb muscles, we first injected pseudorabies virus (PRV), which encoded EGFP, directly into the tibialis anterior/gastrocnemius (TA/GS) muscle. This allowed for the retrograde trans-synaptic labeling of upstream neurons. The ClearMap[31,32] method was utilized for automatic analysis and registration of volumetric data from cleared tissues 5.5 days after viral injection (see STAR Method). The reconstructed whole-brain data of labelled neurons were registered onto the standard Allen CCFv3 map, which showed a widespread distribution of PRV-labeled neurons across the brain (Fig. 1a and Supplementary Video 1). Further analysis revealed that labeled neurons were widely distributed across the hypothalamus, with the highest density of these neurons (36.6% of the total) in the LHA (Fig. 1b–d and Supplementary Fig. 1a, b).

Further kernel density estimation (KDE) of trans-synaptically retrogradely labeled neurons indicated that the highest density of labeled neurons was located in the caudal region of LHA (cLHA, Fig. 1e), which contains both excitatory and inhibitory neurons[33]. Further experiments on optogenetic stimulation of *Vglut2*-ChR2 expressing neurons in 10 hypothalamic nuclei in free-moving mice (Supplementary Fig. 1c–e) revealed that only the activation of LHA *Vglut2*$^+$ neurons resulted in robust locomotion of the mice, in a frequency- and light intensity-dependent manner (Fig. 1f–h) (Ligh intensity: One-way ANOVA $F(5, 30) = 77.32$ with $p < 0.0001$, followed by Dunnett's multiple comparison to 0.1 mW, vs 1 mW $p = 0.0034$, and different from all other groups with $p < 0.0001$. Frequency: One-way ANOVA $F(4, 25) = 19.11$ with $p < 0.0001$, followed by Dunnett's multiple comparison to 0.1 Hz, different from all other groups with $p < 0.0001$.) Thus, LHA *Vglut2*$^+$ neurons represent the main population of hypothalamic neurons that are involved in regulating locomotion in mice.

LHA glutamatergic neurons regulate motivation-driven locomotion

To further understand how the firing rate of LHA neurons is related to locomotion speed, we performed single-unit recording at the caudal LHA of C57BL/6 mice walking on a linear track (1.5 m × 15 cm × 20 cm) using an 8-tetrode drivable array. A total of 156 neurons were recorded from 7 mice. Figure 1i shows an example neuron whose firing rate was positively correlated with speed. To minimize resting-state contamination, we applied a speed filter (excluding epochs below 5 cm/s)[34] and found that 37 neurons (23.7% of the recorded cells) exhibited firing rates that were significantly modulated by locomotion speed (Spearman's correlation, $p < 0.01$; median $p = 0.42$) (Fig. 1j). We subsequently applied two widely recognized criteria to categorize these neurons into putative principal cells, inferred to be glutamatergic neurons, and putative interneurons, believed to be GABAergic neurons[35–37]. Out of these 37 neurons, 24 neurons exhibited characteristics of putative glutamatergic neurons, 3 neurons exhibited characteristics of GABAergic neurons, and the remaining 10 neurons were indistinguishable (Supplementary Fig. 1f). Moreover, a subpopulation of neurons was found to exhibit an increased firing rate prior to the onset of locomotion (Fig. 1k). The LHA is known to be critical for regulating various locomotion-dependent physiological and behavioral functions, including predatory attack, evasion, and other motivated behaviors[9,38,39]. This functional diversity may arise from the heterogeneous cell populations and complex cytoarchitecture within the region. To investigate the association of excitatory versus inhibitory LHA neurons with motivation, we applied fiber photometry to record the Ca^{2+} signals of LHA neurons during food seeking. We injected AAV-DIO-GCaMP6s into the LHA of *Vglut2-Cre* or *Vgat-Cre* mice, allowing for the expression of GCaMP6s specifically in either excitatory or inhibitory LHA neurons, thereby facilitating fiber photometry imaging. We observed an increase of Ca^{2+} signals of excitatory neurons that was time locked to the onset of locomotion, with elevated activity during food seeking behavior when approaching the food. However, these signals decreased during the consumption period (Fig. 1l, m) (From resting to locomotion: $p = 0.0002$, two-tailed, *t*-test with Welch's correction, $t = 7.064$, $df = 6.746$. From food seeking to consumption: $p < 0.0001$, two-tailed, *t*-test, $t = 6.080$, $df = 12$.). LHA inhibitory neurons, on the other hand, did not respond to the onset of locomotion and food-seeking behavior; but their Ca^{2+} activity increased during food consumption (Supplementary Fig. 1g, h) (From resting to locomotion: $p = 0.6226$, two-tailed, *t*-test, $t = 0.5052$, $df = 12$. From food seeking to consumption: $p < 0.0001$, two-tailed, *t*-test, $t = 10.98$, $df = 12$.). Moreover, in open field test, optical stimulation of LHA *Vgat*$^+$ neurons did not induce locomotion in freely-moving mice (Supplementary Fig. 1i) (Maximum speed: $p = 0.3904$, two-tailed, t-test, $t = 0.8978$, $df = 10$. Total distance: $p = 0.3985$, two-tailed, t-test, $t = 0.8819$, $df = 10$.).

To further explore the role of LHA *Vglut2*$^+$ neurons in basic locomotor function and motivated locomotion (e.g., food-seeking), we

https://doi.org/10.1038/s41467-025-67133-5

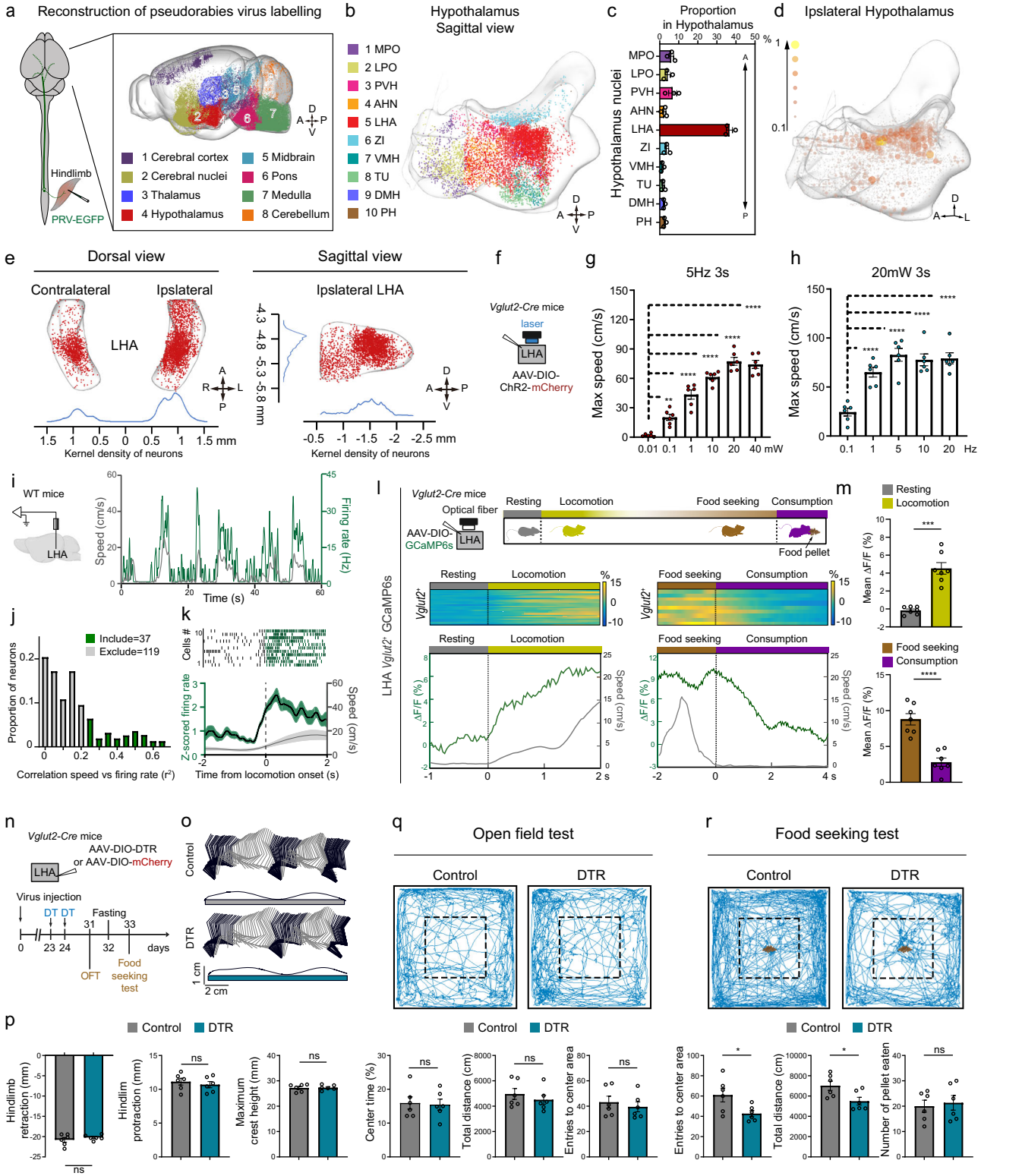

expressed the diphtheria toxin (DT) receptor (DTR) by infusing AAV-DIO-DTR-mCherry vectors into LHA of *Vglut2*⁺-Cre mice (Fig. 1n). DT administration induced neuronal ablation in DTR-expressing mice but not in mCherry expressing control mice (Supplementary Fig. 1j) (mCherry⁺ cell numbers/section: $p < 0.0001$, two-tailed, t-test, t = 11.31, df = 10.). After ablation of LHA excitatory neurons, no significant changes were observed in basic locomotor functions such as hindlimb protraction, retraction and maximum iliac crest height (Fig. 1o, p), suggesting that the ablation of LHA glutamatergic neurons did not impact basic locomotion (Hindlimb retraction: $p = 0.3885$, two-tailed, t-test, t = 0.9016, df = 10. Hindlimb protraction: $p = 0.5318$, two-tailed, t-test, t = 0.6477, df = 10. Maximum iliac crest height: $p = 0.8871$, two-tailed, t-test, t = 0.1456, df = 10.). The ablation of LHA excitatory neurons resulted in no significant change in overall activity in an open field setting (Fig. 1q) (Center time: $p = 0.8479$, two-tailed, t-test, t = 0.1969, df = 10. Total distance: $p = 0.4368$, two-tailed, t-test, t = 0.8100, df = 10. Entries to center area: $p = 0.5639$, two-tailed, t-test, t = 0.5968, df = 10.) However, in the open field chamber in which food pellets were placed

Fig. 1 | LHA glutamatergic neurons in the hypothalamus are predominantly involved in hindlimb motor control and required for motivation-driven locomotion. a Left: Schematic of PRV-EGFP injection into the TA (tibialis anterior muscle) and GS (Gastrocnemius muscle). Right: Reconstruction of adult wild-type mouse brain labeled for EGFP after a viral delivery of PRV in the hindlimb muscle. **b** Reconstruction of PRV-EGFP labelled neurons in the hypothalamus innervating the hindlimb muscles. **c** The percentage of labelled neurons in the hypothalamus ($n = 3$). Error bars, SEM. **d** Three-dimensional heatmap distribution of PRV-labeled cells within the hypothalamus. **e** The dorsal view (left) and sagittal view (right) of PRV-infected lateral hypothalamus area neurons. **f** Strategy for activating LHA glutamatergic neurons. **g**, **h** Quantification of maximum speed corresponding to optical stimulation in different light intensities and frequencies ($n = 6$). One-way ANOVA, followed by followed by Dunnett's multiple comparison. $^{**}p < 0.01$; $^{****}p < 0.0001$. Error bars, SEM. **i** Left: Schematic of tetrode recording for LHA neurons and offline spike sorting. Right: Firing rate of one representative neuron in LHA (green line, right axis) plotted with the speed (gray line, left axis) of the mouse. **j** Distribution of the recorded LHA neurons showing the speed of locomotion based on their relative correlation (r^2) with speed. Green bars, speed-correlated neurons; Gray bars, neurons show no significant correlation with the speed. **k** Top: Raster plot for spike responses of representative neurons to locomotion onset. Bottom: population z-scored firing rate of a subpopulation LHA neurons (green line) and speed (gray line) aligned to the onset of locomotion. Error bars, SEM. **l** Top: Strategy for fiber photometry recording of LHA *Vglut2*$^+$ neurons and food seeking test in the runway. Bottom: Calcium dynamics of LHA *Vglut2*$^+$ neurons in response to onset of locomotion and consumption. m, Quantification of LHA *Vglut2*$^+$ neurons calcium response to onset of locomotion (top) and food consumption (bottom). $n = 7$ mice, 3-5 trials per mouse. Student's *t*-test (two-tailed, unpaired) was applied. $^{***}p < 0.001$; $^{****}p < 0.0001$. Error bars, SEM. **n** Timeline summarizing the experiments of gait analysis, open field and food seeking test with or without depletion of LHA glutamatergic neurons. **o** Representative stick diagram decomposition of leg movements in mice with or without depletion of LHA glutamatergic neurons. **p** Quantification of retraction, protraction and height of iliac crest with or without depletion of LHA glutamatergic neurons ($n = 6$). Student's *t*-test (two-tailed, unpaired) was applied. ns not significant. Error bars, SEM. **q** Top: Trajectory of mice in open-field chambers with or without depletion of LHA glutamatergic neurons. Bottom: Quantification of center time, total distance and entries to center area ($n = 6$). Student's *t*-test (two-tailed, unpaired) was applied. ns, not significant. Error bars, SEM. r, Top: Trajectory of mice in open-field chambers with food pellets placed in the center before and after the depletion of LHA glutamatergic neurons. Bottom: Quantification of entries to center area, total distance, and number of food pellets consumed by mice in open-field chambers with food pellets placed in the center ($n = 6$). Student's *t*-test (two-tailed, unpaired) was applied. $^{*}p < 0.05$. Error bars, SEM. Source data are provided as a Source data file.

in the center, the locomotor activity was reduced and the mice were less likely to enter the center area, even though their appetite, as measured by food pellet consumption, was not affected (Fig. 1r) (Entries to center area: $p = 0.0332$, two-tailed, t-test, $t = 2.468$, $df = 10$. Total distance: $p = 0.0281$, two-tailed, t-test, $t = 2.565$, $df = 10$. Number of pellet eaten: $p = 0.7288$, two-tailed, t-test, $t = 0.3566$, $df = 10$.). Together, these results suggest that LHA neurons play a vital role in regulating motivational locomotion.

LHA neurons regulate locomotion via projections to PnO and MSDB

We next explored the circuit mechanism underlying the function of LHA projection in locomotion control. We searched in a single-neuron projectome dataset for mouse LHA for the major brain regions receiving axon projections from LHA neurons[40]. This dataset consists of single-axon tracing of 916 sparsely labelled neurons expressing various neuropeptides (Supplementary Fig. 2a). To classify the pattern of axon projections of these neurons, we calculated similarity scores based on the shortest distances between neuron pairs. We then performed hierarchical clustering of the similarity matrix of all neuron pairs using Ward's linkage. Using this approach, we categorized lateral hypothalamus neurons into 4 main clusters and 7 projectome-defined subtypes (Fig. 2a, b and Supplementary Fig. 2b), with subtypes 1 and 2 in the rostral projecting cluster (Cluster 1, ~16% of the total neurons), subtype 3 in the local projecting cluster (Cluster 2, ~13% of the total neurons), subtypes 4 and 5 in the caudal projecting cluster (Cluster 3, ~46% of the total neurons), and subtypes 6 and 7 in the long-distance projecting cluster (Cluster 4, ~25% of the total neurons).

Among the neurons that were grouped into subtypes 1 and 2 of the rostral projecting cluster (Cluster 1), most neurons displayed targeting preferences for thalamus (TH) and cerebral nuclei (CNU), respectively. Notably, a distinct subgroup within Subtype 1 (TH-projecting) specifically projected to the lateral habenula (LHb). Subtype 2 exhibited strong projections to the cerebral nuclei (CNU), including lateral septal nucleus (LS), bed nuclei of the stria terminalis (BST), substantia innominate (SI), and medial septum and diagonal band of Broca (MSDB). Cluster 2 consisted of subtype 3, which primarily projected within the hypothalamus with short axons. By comparison, the midbrain-projecting subtype 4 in cluster 3 projected with varying strengths to the periaqueductal gray (PAG) and superior colliculus (SCm) in the midbrain. Neurons in subtype 5 within cluster 3 primarily terminated their axons within the pontine, including PnO, parabrachial nucleus (PB), laterodorsal tegmental nucleus (LDT), and pontine central gray (PCG). Cluster 4 neurons had broader projections over longer distances, with subtype 6 projecting specifically to the cortex and the medulla, while subtype 7 was more medulla-specific. Among cluster 4 neurons, nearly half (111 out of 233) of the neurons had direct projections to the spinal cord (Supplementary Fig. 2b).

Given that optogenetic activation of LHA glutamatergic neurons elicited hindlimb locomotion, we examined whether those neurons that projected directly to the lumbar spinal cord circuits (Fig. 2c) might generate rhythmic motor patterns. The results from anterograde tracing demonstrated that LHA glutamatergic neurons projected robustly to the dorsal part of lumbar spinal cord (Fig. 2d, e). Retrograde labeling also demonstrated the existence of spinal-projecting LHA glutamatergic neurons (Fig. 2f). To explore the function of the LHA-spinal cord pathway, we expressed ChR2 in excitatory spinal cord-projecting LHA neurons by injecting retrogradely transported AAV-expressing Cre-dependent ChR2 into the spinal cord and implanting optical fibers in the LHA of *Vglut2-Cre* mice. We found that optogenetic stimulation of these spinal cord-projecting LHA neurons did not elicit locomotor behaviors (Fig. 2i–k). This indicates that an indirect pathway from LHA to spinal cord might be involved.

On the basis of our hierarchical clustering analysis, anterograde tracing results and previous research in motor control[1,4–6,41,42], we selected 3 potential downstream brain regions that receive projections from the rostral LHA neurons, including the LS, MSDB, and BST, as well as 7 downstream brain regions that receive projections from the caudal LHA neurons, including the substantia nigra reticular part (SNr), PB, LDT, PnO, PCG, gigantocellular reticular nucleus (Gi), and lateral paragigantocellular nucleus (LPGi), to determine their roles in locomotion (Fig. 2g, h and Supplementary Fig. 2c). This was achieved by injecting AAVs carrying Cre-dependent ChR2-mCherry into the LHA of *Vglut2-Cre* mice and stimulating the axonal terminals of LHA neurons in these downstream brain regions across the brain (Fig. 2i). Optogenetic activation of axon terminals of LHA neurons in these different regions resulted in varying effects on the mouse locomotion. Notably, activation of LHA neuron projection to the PnO or MSDB could initiate locomotion, whereas MSDB activation led to high-speed locomotion, in contrast to the more moderate responses elicited by PnO activation (Fig. 2j, k and Supplementary Video 2 and 3) (Total distance: One-way ANOVA $F(11, 60) = 265.0$ with $p < 0.0001$, followed by Dunnett's multiple comparison to SC, different from LHA soma, MSDB and PnO with $p < 0.0001$. Maximum speed: One-way ANOVA $F(11, 60) = 151.2$ with

https://doi.org/10.1038/s41467-025-67133-5

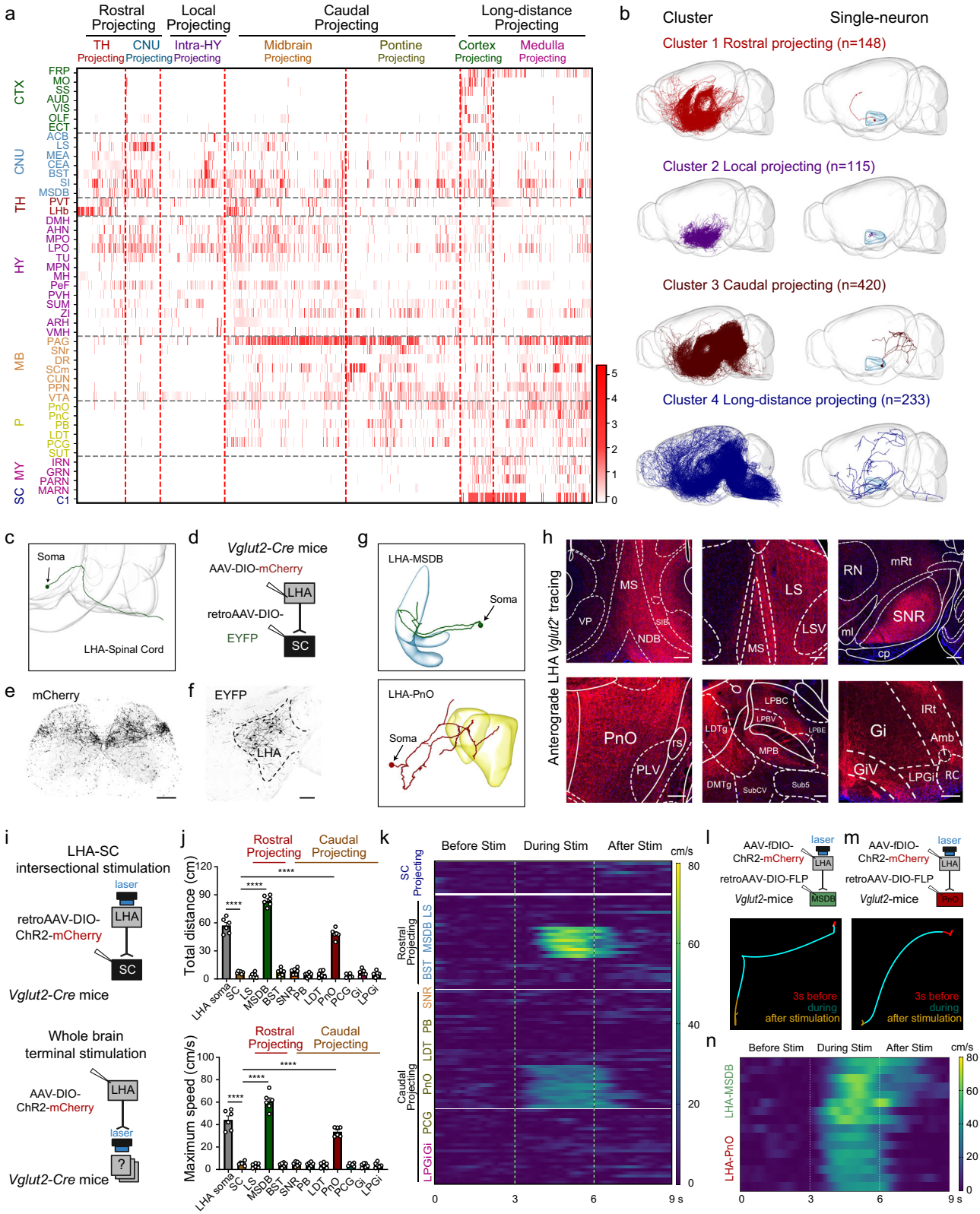

$p < 0.0001$, followed by Dunnett's multiple comparison to SC, different from LHA soma, MSDB and PnO with $p < 0.0001$.).

To further validate the involvement of the LHA-PnO and LHA-MSDB projections in locomotion, we injected retrogradely transported AAVs carrying Cre into the PnO and MSDB, respectively, while expressing Cre-dependent ChR2 in the LHA of wild-type mice. Stimulation of the cell bodies of LHA neurons projecting to PnO or MSDB successfully induced locomotion in freely moving mice (Supplementary Fig. 2d–h) (LHA-MSDB maximum speed: $p < 0.0001$, two-tailed with Welch's correction, t-test, t = 26.32, df = 5.721. LHA-MSDB total distance: $p < 0.0001$, two-tailed with Welch's correction, t-test, t = 22.47, df = 5.121. LHA-PnO maximum speed: $p < 0.0001$, two-tailed with Welch's correction, t-test, t = 14.70, df = 5.273. LHA-PnO total distance: $p < 0.0001$, two-tailed, t-test, t = 15.37, df = 10.). To further

Fig. 2 | Single-neuron projectome-guided analysis of neural circuits underlying LHA circuit in locomotion control. a Projection strength of 916 LHA neurons arranged according to the clustering assignment. Each column represents a neuron. Each row represents a brain region, and the heatmap colors indicate projection strength. **b** Sagittal views of the morphology of all neurons (left) and the example neuron (right) of four classes of LHA neurons. **c** Sagittal views of the morphology of a spinal projecting LHA neuron. **d** Strategy for viral injection to demonstrate the existence of LHA-spinal cord circuit. **e** LHA excitatory projections in lumbar spinal cord. Scale bar, 200 μm. **f** Representative image showing spinal cord-projecting LHA glutamatergic neurons. Scale bar, 200 μm. **g** The morphology of representative neurons in the LHA projecting to MSDB (top) and PnO (bottom). **h** Representative images showing different downstream regions of LHA *Vglut2*$^+$ neurons from anterograde axonal AAV-DIO-ChR2-mCherry tracing. Scale bar, 200 μm. **i** Strategy for activation of spinal cord-projecting LHA glutamatergic neurons (top) and terminal stimulation of downstream brain regions (bottom). **j** Quantification of total distance and maximum speed corresponding to optogenetic activation. One-way ANOVA, followed by followed by Dunnett's multiple comparison. $n = 3$ attempts per mouse; $n = 6$ mice per group. $^{****}p < 0.0001$. Error bars, SEM. **k** Heatmap illustrating speed versus time during optical stimulation of LHA neurons projecting to spinal cord and other downstream brain regions. **l** Top: Strategy for activating MSDB projecting LHA neurons in *Vglut2*-cre mice. Bottom: Centre of body mass trajectories of single trials in open field arena during 3-s time windows: stationary phase (red), stimulation phase (cyan) and after stimulation offset (orange). **m** Top: Strategy for activating PnO projecting LHA neurons in *Vglut2*-cre mice. Bottom: Centre of body mass trajectories of single trials in open field arena during 3-s time windows: stationary phase (Red), stimulation phase (cyan) and after stimulation offset (orange). **n** Heatmap illustrating speed versus time during optical stimulation of MSDB and PnO-projecting LHA excitatory neurons. Source data are provided as a Source data file.

confirm the functional role of LHA glutamatergic projections to the MSDB/PnO, we employed an intersectional optogenetic strategy in *Vglut2*-Cre mice by injecting RetroAAV-DIO-FLP into the PnO or MSDB and AAV-fDIO-ChR2 into the LHA, followed by optical stimulation in the LHA. Importantly, this approach robustly induced locomotion, which was consistent with our original findings in WT mice (Fig. 2l–n and Supplementary Fig. 2i, j) (LHA-MSDB maximum speed: $p < 0.0001$, two-tailed with Welch's correction, t-test, t = 17.57, df = 5.479. LHA-MSDB total distance: $p < 0.0001$, two-tailed with Welch's correction, t-test, t = 17.90, df = 5.704. LHA-PnO maximum speed: $p < 0.0001$, two-tailed with Welch's correction, t-test, t = 10.30, df = 5.880. LHA-PnO total distance: $p = 0.0003$, two-tailed with Welch's correction, t-test, t = 8.279, df = 5.444.).

Given that low speed locomotion is controlled by the caudal PPN[5,23,34,43], we tested the potential role of PPN glutamatergic neurons in mediating LHA-PnO induced locomotion. The PPN glutamatergic neurons were selectively silenced by bilaterally injecting AAV-DIO-hM4Di into the caudal PPN of *Vglut2*-Cre mice and administering CNO before locomotor testing (Supplementary Fig. 2k, l). LHA-PnO optogenetic stimulation still evoked locomotion even after PPN glutamatergic neurons inhibition (Supplementary Fig. 2m, n) (Maximum speed: $p = 0.6738$, two-tailed, t-test, t = 0.4335, df = 10. Total distance: $p = 0.7968$, two-tailed, t-test, t = 0.2645, df = 10.). These results demonstrate that LHA-PnO projections can drive locomotion independently of PPN glutamatergic neurons, further supporting our conclusion that the LHA-PnO pathway is crucial for locomotion initiation. Collectively, these results demonstrate that the projections from the LHA to the PnO or MSDB play a crucial role in regulating locomotion.

LHA-PnO neurons facilitate motivation-driven locomotion without inducing anxiety

Next, we investigated the differential roles of MSDB-projecting and PnO-projecting LHA neurons in regulating mouse locomotion. Our findings demonstrated that optical stimulation of MSDB-projecting LHA neurons elicited high-speed running that resembled escape behavior, a response distinct from that observed following stimulation of LHA-PnO projections (Fig. 2j, k). Further open field test and elevated plus-maze test for the stress response of the mice indicated that stimulation of MSDB-projecting LHA neurons resulted in a significant reduction in the time spent in the center during the open field test and in the time in the open arms during the elevated plus-maze test. In contrast, stimulation of LHA-PnO axon terminals did not elicit any significant stress response (Fig. 3a–c) (LHA-MSDB OFT center time: One-way ANOVA F(2, 15) = 21.50 with $p < 0.0001$, followed by Tukey's multiple comparison, before vs during stim $p < 0.0001$, before vs after stim $p = 0.0004$, and during vs after stim $p = 0.5784$. LHA-MSDB OFT total distance: One-way ANOVA F(2, 15) = 23.19 with $p < 0.0001$, followed by Tukey's multiple comparison, before vs during stim $p = 0.002$, before vs after stim $p = 0.0572$, and during vs after stim $p < 0.0001$. LHA-MSDB OFT entries to center area: One-way ANOVA F(2, 15) = 14.42 with $p = 0.0003$, followed by Tukey's multiple comparison, before vs during stim $p = 0.0007$, before vs after stim $p = 0.001$, and during vs after stim $p = 0.9794$. LHA-PnO OFT center time: One-way ANOVA F(2, 15) = 1.512 with $p = 0.2522$. LHA-PnO OFT total distance: One-way ANOVA F(2, 15) = 4.466 with $p = 0.0301$, followed by Tukey's multiple comparison, before vs during stim $p = 0.0236$, before vs after stim $p = 0.3771$, and during vs after stim $p = 0.2725$. LHA-PnO entries to center area: One-way ANOVA F(2, 15) = 20.57 with $p < 0.0001$, followed by Tukey's multiple comparison, before vs during stim $p < 0.0001$, before vs after stim $p = 0.006$, and during vs after stim $p = 0.4792$. LHA-MSDB EPM center time: One-way ANOVA F(2, 15) = 40.55 with $p < 0.0001$, followed by Tukey's multiple comparison, before vs during stim $p < 0.0001$, before vs after stim $p < 0.0001$, and during vs after stim $p = 0.5430$. LHA-MSDB EPM total distance: One-way ANOVA F(2, 15) = 10.02 with $p = 0.0017$, followed by Tukey's multiple comparison, before vs during stim $p = 0.0433$, before vs after stim $p = 0.2118$, and during vs after stim $p = 0.0013$. LHA-PnO EPM center time: One-way ANOVA F(2, 15) = 1.629 with $p = 0.2290$. LHA-PnO EPM total distance: One-way ANOVA F(2, 15) = 3.640 with $p = 0.0515$, followed by Tukey's multiple comparison, before vs during stim $p = 0.0413$, before vs after stim $p = 0.4069$, and during vs after stim $p = 0.3761$. Notably, during the food-seeking test, optogenetic activation of the LHA-PnO pathway increased the number of entries into the center zone without affecting food consumption, whereas stimulation of LHA-MSDB terminals produced the opposite behavioral effect, significantly reducing center entries (Supplementary Fig. 3b, c) (LHA-MSDB entries to center area: $p = 0.0028$, two-tailed, t-test, t = 3.931, df = 10. LHA-MSDB total distance: $p = 0.2008$, two-tailed, t-test, t = 1.369, df = 10. LHA-MSDB pellet eaten: $p = 0.8376$, two-tailed, t-test, t = 0.2104, df = 10. LHA-PnO entries to center area: $p = 0.0252$, two-tailed, t-test, t = 2.629, df = 10. LHA-PnO total distance: $p = 0.2954$, two-tailed, t-test, t = 1.104, df = 10. LHA-PnO pellet eaten: $p = 0.5732$, two-tailed, t-test, t = 0.5824, df = 10.). Through injecting retrogradely transported AAVs carrying Cre into the PnO or the MSDB, while expressing Cre-dependent DTR in the LHA of wild-type mice, we found that depletion of PnO-projecting rather than MSDB-projecting LHA neuron impaired motivation-driven locomotion, as indicated by the reduced total distance and entries to the center compared to the control group (Fig. 3d, e) (LHA-MSDB entries to center area: $p = 0.4456$, two-tailed, t-test, t = 0.7941, df = 10. LHA-MSDB total distance: $p = 0.4755$, two-tailed, t-test, t = 0.7414, df = 10. LHA-MSDB pellet eaten: $p = 0.7094$, two-tailed, t-test, t = 0.3835, df = 10. LHA-PnO entries to center area: $p = 0.0051$, two-tailed, t-test, t = 3.571, df = 10. LHA-PnO total distance: $p = 0.0293$, two-tailed, t-test, t = 2.541, df = 10. LHA-PnO pellet eaten: $p = 0.3122$, two-tailed, t-test, t = 1.064, df = 10.). However, ablation of MSDB- or PnO-projecting LHA neurons did not significantly alter general locomotor activity in the open field test nor anxiety-like

https://doi.org/10.1038/s41467-025-67133-5

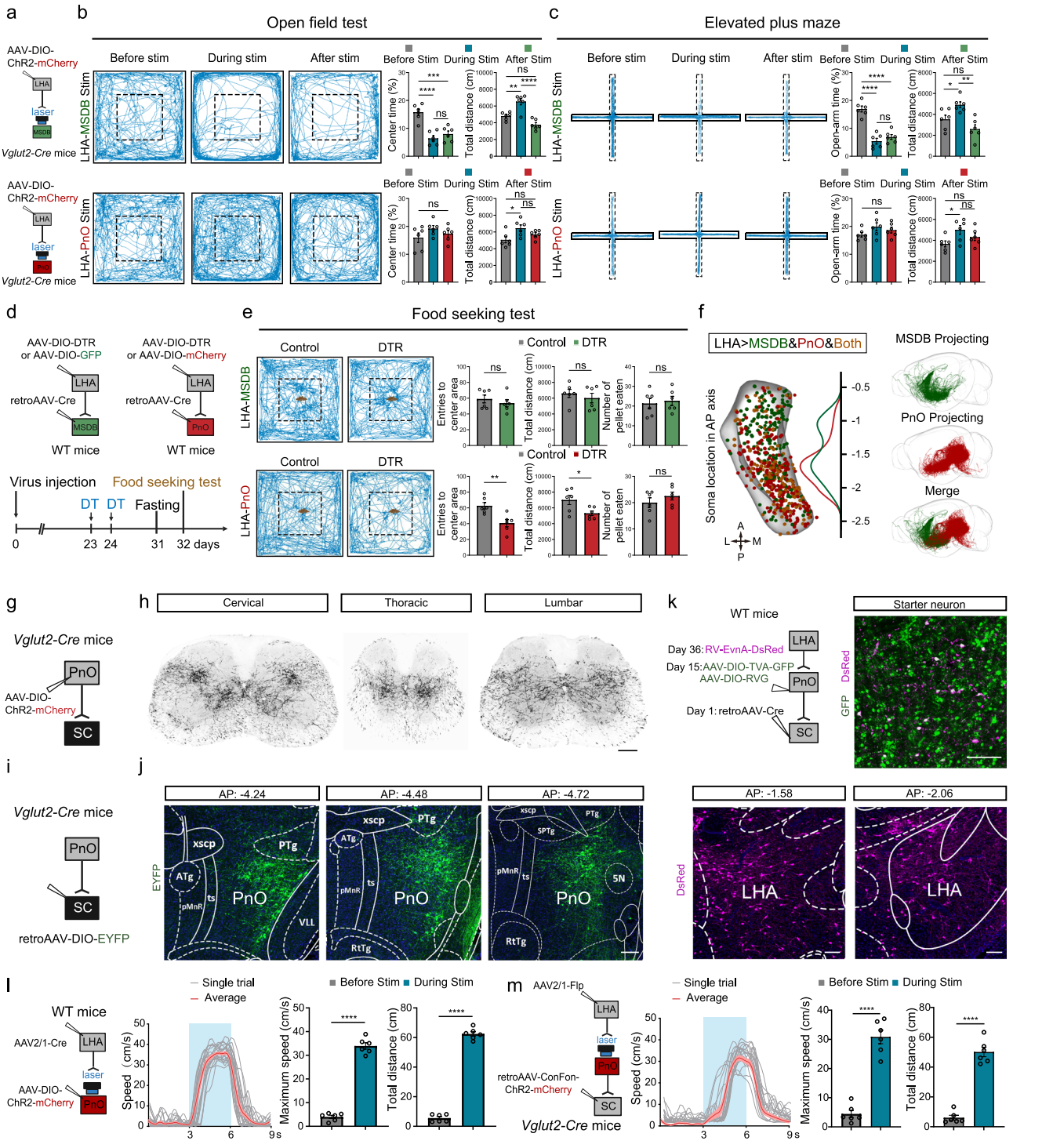

behavior in the elevated plus-maze (Supplementary Fig. 3d–f) (LHA-MSDB OFT center time: $p = 0.9432$, two-tailed, t-test, t = 0.07311, df = 10. total distance: $p = 0.9087$, two-tailed, t-test, t = 0.1176, df = 10. Entries to center area: $p = 0.7666$, two-tailed, t-test, t = 0.3050, df = 10. LHA-MSDB EPM open arm time: $p = 0.6752$, two-tailed, t-test, t = 0.4316, df = 10. total distance: $p = 0.9433$, two-tailed, t-test, t = 0.07293, df = 10. LHA-PnO OFT center time: $p = 0.8747$, two-tailed, t-test, t = 0.1618, df = 10. total distance: $p = 0.8570$, two-tailed, t-test, t = 0.1848, df = 10. Entries to center area: $p = 0.9585$, two-tailed, t-test, t = 0.05341, df = 10. LHA-MSDB EPM open arm time: $p = 0.7860$, two-tailed, t-test, t = 0.2789, df = 10. total distance: $p = 0.8669$, two-tailed, t-test, t = 0.1720, df = 10.). Immunohistochemical analysis confirmed efficiency of ablation of LHA-PnO projecting neurons (Supplementary Fig. 3g) (mCherry$^+$ cell numbers/section: $p < 0.0001$, two-tailed, t-test, t = 8.179, df = 10). Collectively, the data demonstrated that while LHA neurons are dispensable for baseline locomotor activity, the LHA-PnO pathway was specifically required for motivation-driven locomotion during food-seeking behavior. These findings establish the LHA-PnO circuit as a dedicated neural substrate that selectively transforms motivational signals into locomotor output, without affecting general movement. Further examination of the soma distribution of neurons projecting to these two brain areas in single-neuron projectome data showed that somata for these two distinct projections exhibited a spatially distinct anterior-posterior arrangement (Fig. 3f and Supplementary Fig. 3h). According to the connectome data, different projecting clusters exhibited distinct peptidergic signatures

Fig. 3 | The LHA-PnO-spinal pathway is essential for relaying locomotor signals from the hypothalamus to the spinal cord. a Strategy for terminal stimulation of LHA-MSDB and LHA-PnO pathways. **b** Left: Locomotion tracing for an example animal of LHA-MSDB (top) or LHA-PnO (bottom) terminal stimulation in the OFT. Right: Quantification of center time and total distance of LHA-MSDB (top) or LHA-PnO (bottom) terminal stimulation in the OFT ($n = 6$). One-way ANOVA/Tukey's multiple comparison was applied. ns, not significant; $^{*}p < 0.05$; $^{**}p < 0.01$; $^{***}p < 0.001$; $^{****}p < 0.0001$. Error bars, SEM. **c** Left: Locomotion tracing for an example animal of LHA-MSDB (top) or LHA-PnO (bottom) terminal stimulation in the EPM. Right: Quantification of center time and total distance of LHA-MSDB (top) or LHA-PnO (bottom) terminal stimulation in the EPM ($n = 6$). One-way ANOVA/Tukey's multiple comparison was applied. ns not significant; $^{*}p < 0.05$; $^{**}p < 0.01$; $^{****}p < 0.0001$. Error bars, SEM. **d** Strategies and timeline summarizing the experiments of food seeking test with or without depletion of MSDB or PnO projecting LHA neurons. **e** Left: Trajectory of mice in open-field chambers with food pellets placed in the center with or without the depletion of MSDB-projecting or PnO-projecting LHA neurons. Right: Quantification of entries to center area, total distance and number of food pellets consumed by mice in open-field chambers ($n = 6$). Student's t-test (two-tailed, unpaired) was applied. ns, not significant; $^{*}p < 0.05$; $^{**}p < 0.01$. Error bars, SEM. **f** Left: Soma location of MSDB (green) and PnO projecting (red) LHA neurons. Right: Reconstructions of MSDB-projecting neurons in subtype 2 and PnO-projecting neurons in subtype 5. **g** Strategy for anterograde labeling of glutamatergic PnO neurons. **h** Representative confocal images showing the expression of mCherry within spinal cord. Scale bar, 200 μm. **i** Strategy for retrograde labeling glutamatergic spinal cord-projecting PnO neurons. **j** Representative confocal images showing the expression of EYFP at indicated positions within PnO. Scale bar, 200 μm. **k** Schematic of three-step monosynaptic rabies virus tracing strategy to demonstrate the circuit of LHA-PnO-spinal cord and trans-synaptically labelled neurons were found in the LHA. Scale bar, 200 μm. **l** Strategy for activation of PnO-projecting LHA neurons. Speed versus time of single trials (grey lines) and the average (red line) of one mouse. Quantification of total distance (left) and maximum speed (right) of mice before and during optical stimulation ($n = 6$). Student's t-test (two-tailed, unpaired) was applied. $^{****}p < 0.0001$. Error bars, SEM. m, Strategy for activation of LHA-PnO^{Vglut2}-Spinal cord. Speed versus time of single trials (grey lines) and the average (red line) of one mouse. Quantification of total distance (left) and maximum speed (right) of mice before and during optical stimulation ($n = 6$). Student's t-test (two-tailed, unpaired) was applied. $^{****}p < 0.0001$. Error bars, SEM. Source data are provided as a Source data file.

(Supplementary Fig. 3i). Approximately 48.99% of neurons that project to the spinal cord express *Orexin*, while neurons projecting to the PnO and MSDB comprise a heterogeneous population of peptidergic neurons. Axonal collaterals play a crucial role in neuronal communication, allowing for the integration of signals across different regions. Topographic arrangements of individual PnO-projecting neuron revealed the existence of axon collaterals in both PPN and VTA (Ventral tegmental area), which have been reported to play roles in locomotion and motivational circuits, respectively (Supplementary Fig. 3j)[5,6,9]. A strategy for intersectional viral screening was also performed to identify collateral innervation of PnO-projecting LHA neurons. RetroAAV-Cre was injected in PnO, followed by injection of AAV-DIO-mChery in LHA. Labeling of PnO-projecting LHA neurons revealed collateral axonal processes in the VTA and PPN (Supplementary Fig. 3k). These findings indicate a complex interplay between axonal projection patterns, somatic locations, and neuropeptide expression, which are intrinsic features of specific neuronal populations. Therefore, integrating projectome-defined subtypes with molecular markers and somatic locations is expected to enhance our understanding of the distinct neuronal subtypes that are involved in diverse hypothalamic functions.

Activation of the LHA-PnO-Spinal pathway initiates locomotion

Our anterograde tracing experiment showed that PnO comprised a majority of pontine reticulospinal neurons which directly projected to the spinal cord (Fig. 3g, h). Through retrogradely labeling from the lumbar spinal cord, we found that somata of spinal-projecting PnO excitatory neurons were mainly located in the lateral part of PnO (Fig. 3i, j). To demonstrate the role of PnO as a relay station connecting LHA and lumbar spinal cord, AAVretro-DIO-EYFP was injected into lumbar spinal cord, followed by an anterograde tracing virus AAV-DIO-mCherry injected into LHA. Double positive signals were identified in PnO (Supplementary Fig. 3l). Moreover, we performed rabies virus-based three-step monosynaptic retrograde tracing experiments. Specifically, retroAAV-hSyn-Cre was delivered into the lumbar spinal cord, followed by the injection of AAVs expressing Cre-dependent avian-specific retroviral receptor (TVA) and rabies virus glycoprotein (RVG) into the PnO 2 weeks later. RV-EnvA-dsRed was then delivered into PnO, and neurons expressing both EGFP and dsRed in PnO represented the "starter cells" in the monosynaptic rabies virus tracing method. Furthermore, trans-synaptically labelled neurons were abundantly found in the LHA (Fig. 3k). These results indicate the existence of LHA-PnO-spinal cord pathway.

We then expressed anterograde trans-synaptic AAVs (AAV serotype 1) carrying Cre into the LHA in WT mice[44–46], alongside AAV encoding Cre-dependent ChR2 in the PnO to stimulate the LHA-recipient PnO neurons. Optogenetic activation of LHA-recipient PnO neurons produced locomotor effects that were similar to those observed when stimulating LHA glutamatergic terminals in the PnO, confirming that the LHA-PnO pathway is crucial for locomotion (Fig. 3l and Supplementary Video 4) (Maximum speed: $p < 0.0001$, two-tailed, t-test, t = 20.18, df = 10. Total distance: $p < 0.0001$, two-tailed, t-test, t = 30.72, df = 10.). To functionally investigate whether the PnO-spinal pathway plays a direct role in locomotor control, we delivered retroAAV-DIO-ChR2 into the spinal cord of *Vglut2-Cre* mice. This retrograde-transported viral construct was specifically taken up by axon terminals of spinally-projecting neurons and transported in a retrograde manner to their cell bodies in the PnO. Following ChR2 expression in retrogradely labeled cell bodies in the PnO, optogenetic stimulation reliably induced locomotion in freely-moving mice (Supplementary Fig. 3m) (Maximum speed: $p < 0.0001$, two-tailed, t-test, t = 13.82, df = 10. Total distance: $p < 0.0001$, two-tailed, t-test, t = 19.43, df = 10.). To further validate the role of LHA-PnO-Spinal cord, we conducted optogenetic experiments in *Vglut2*-cre mice. Specifically, we injected AAV1-FLP into LHA and Retro-ConFon-ChR2 into the spinal cord. Optical stimulation of PnO neurons that both received LHA inputs and projected to the spinal cord evoked locomotion (Fig. 3m) (Maximum speed: $p < 0.0001$, two-tailed, t-test, t = 10.02, df = 10. Total distance: $p < 0.0001$, two-tailed, t-test, t = 12.35, df = 10.). Together, these results indicate that LHA indirectly activate spinal cord neurons through a relay station of PnO to induce locomotion behavior.

LHA-PnO circuit contributes to spontaneous locomotor recovery following incomplete SCI

Our results demonstrated that the LHA-PnO-Spinal descending pathway plays a crucial role in facilitating motivated locomotion in uninjured mice. This prompted us to explore their potential involvement in voluntary locomotion following SCI. We first characterized spontaneous locomotor recovery in mice received a lateral hemisection at the thoracic segment 10 (T10)[21,47]. Three days after injury, mice displayed a complete loss of stepping ability in the ipsilesional hindlimb. In contrast, in the chronic phase after SCI, we observed significant locomotor recovery in all mice, as indicated by body weight-bearing plantar stepping (Supplementary Fig. 4a, b).

Next, we examined whether LHA neurons contribute to the observed locomotor recovery after spinal hemisection by performing two complementary sets of experiments (Fig. 4a, b). Three groups of WT mice received PRV-injection from the hindlimb (GS/TA) muscle and sacrificed 5.5 days after injection: uninjured control mice, mice injected 3 days after injury, and mice injected 8 weeks after injury. In

https://doi.org/10.1038/s41467-025-67133-5

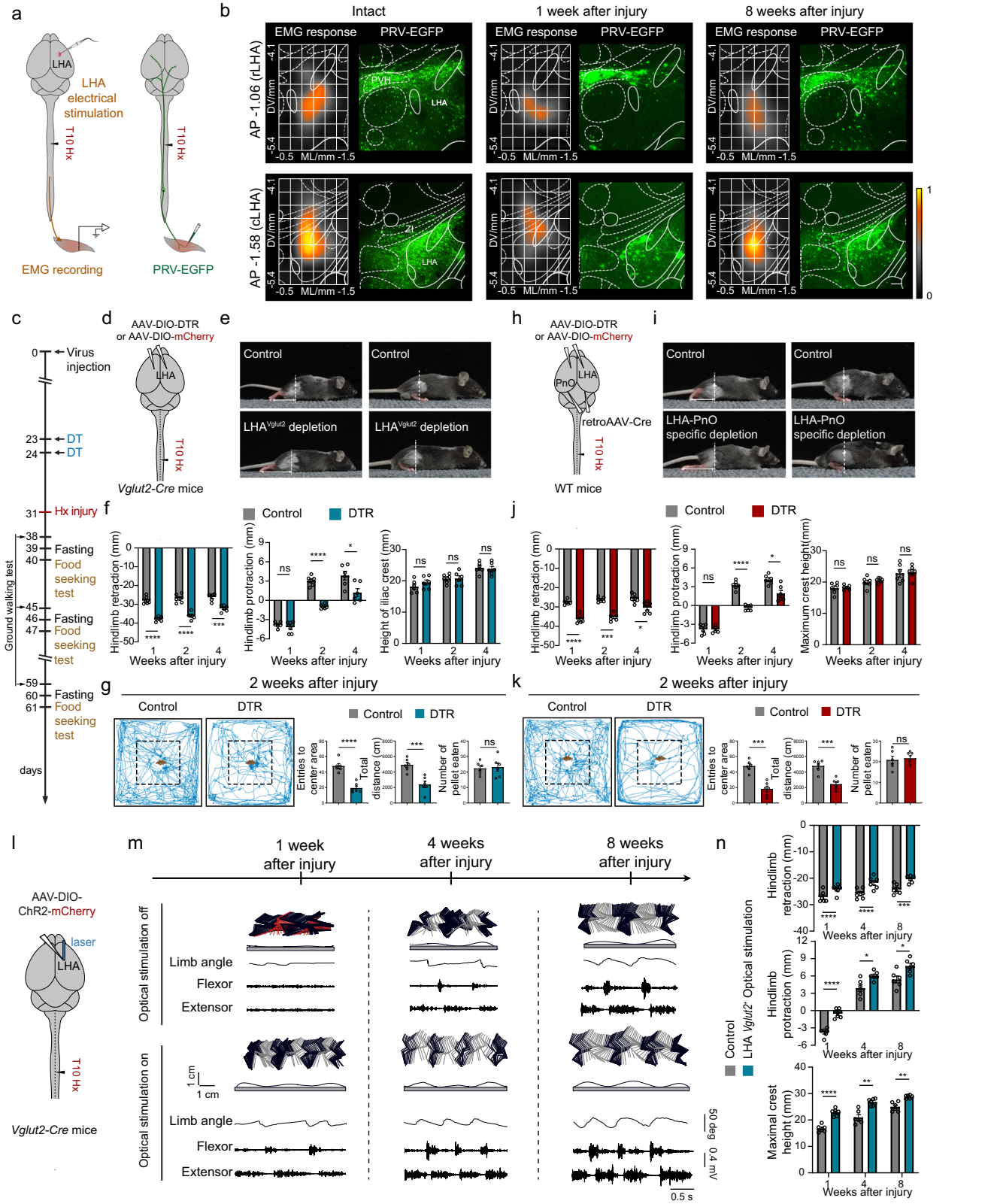

mice that were injected with PRV 3 days post-injury, we found that neuronal labeling in LHA was much lower than that observed in uninjured mice, indicating spinal hemisection disrupted descending projection from LHA to the locomotor circuits below the lesion. In contrast, mice injected with the PRV 8 weeks post-injury demonstrated a significant recovery of labeled neurons in cLHA, but not in rostral LHA (rLHA), suggesting substantial re-establishment of neuronal connections from cLHA to the spinal cord over time after SCI (Fig. 4b and Supplementary Fig. 4c) (One-way ANOVA $F(2, 6) = 7.576$ with $p = 0.0228$, followed by Tukey's multiple comparison, intact vs acute $p = 0.0273$, intact vs chronic $p = 0.8972$, and acute vs chronic $p = 0.0466$. Additionally, we mapped the LHA regions responsible for triggering TA muscle contraction in uninjured mice and injured mice during the early and late post-injury phase under anesthesia. In

Fig. 4 | Functional reorganization of LHA-PnO circuits contributes to spontaneous locomotor recovery. a Strategy for EMG recording of LHA electrical stimulation and trans-synaptic retrograde labeling of hindlimb muscle related neurons. **b** LHA mapping using electrical stimulation (left) and trans-synaptic PRV tracing (right) before injury, at the acute stage (1 week post-injury), or at the chronic stage (8 week post-injury). Scale bar, 200 μm. **c** Timeline for locomotor function test and food seeking test after the conditional genetic ablation of LHA *Vglut2*$^+$ neurons or PnO-projecting LHA neurons in injured mice. **d** Strategy for depletion of LHA *Vglut2*$^+$ neurons in T10 hemisection injury mouse. **e** Example photographs of mice in ground walking, with or without depletion of LHA glutamatergic neurons after lateral hemisection SCI. **f** Quantification of retraction, protraction, and maximum crest height of mice at 1, 2, and 4 week post T10 lateral hemisection ($n = 6$). Two-way RM ANOVA, Geisser-Greenhouse correction followed by Bonferroni's multiple comparison. ns not significant; $^*p < 0.05$; $^{***}p < 0.001$; $^{****}p < 0.0001$. Error bars, SEM. **g** Left: Trajectory of mice in open-field chambers with food pellets placed in the center with or without depletion of LHA glutamatergic neurons after hemisection injury. Right: Quantification of entries to center area, total distance and number of food pellets consumed by mice in open-field chambers with food pellets placed in the center ($n = 6$). Student's t test (two-tailed, unpaired) was applied. ns, not significant; $^{***}p < 0.001$; $^{****}p < 0.0001$. Error bars, SEM. **h** Strategy for depletion of PnO-projecting LHA neurons in T10 hemisection injury mouse. **i** Example photographs of mice in ground walking, with or without depletion of PnO-projecting LHA neurons after lateral hemisection SCI. **j** Quantification of retraction, protraction and maximum crest height of mice at 1, 2, and 4 week post T10 lateral hemisection ($n = 6$). Two-way RM ANOVA, Geisser-Greenhouse correction followed by Bonferroni's multiple comparison. ns, not significant; $^*p < 0.05$; $^{****}p < 0.0001$. Error bars, SEM. **k** Left: Trajectory of mice in open-field chambers with food pellets placed in the center with or without depletion of PnO-projecting LHA neurons after hemisection injury. Right: Quantification of entries to center area, total distance and number of food pellets consumed by mice in open-field chambers with food pellets placed in the center ($n = 6$). Student's *t*-test (two-tailed, unpaired) was applied. ns, not significant; $^{***}p < 0.001$. Error bars, SEM. **l** Strategy for activating glutamatergic LHA neurons. **m** Representative stick diagram decomposition of leg movements, oscillation of the whole limb (virtual limb linking the hip to the toe) and EMG activity of ankle muscles recorded at 1, 4 and 8 week post T10 lateral hemisection with and without optical stimulation of LHA *Vglut2*$^+$ neurons. **n** Quantification of retraction, protraction, and maximum crest height of mice at 1, 4, and 8 week post T10 lateral hemisection ($n = 6$). Two-way RM ANOVA, Geisser-Greenhouse correction followed by Bonferroni's multiple comparison. $^*p < 0.05$; $^{**}p < 0.01$; $^{***}p < 0.001$; $^{****}p < 0.0001$. Error bars, SEM. Source data are provided as a Source data file.

uninjured mice, electrical stimulation of the LHA induced TA muscle contraction. Stimulation at the same LHA subregion failed to produce TA muscle contraction at the early stage (1 week post-injury), but successfully triggered TA muscle activation 8 weeks post-injury (Fig. 4b). This suggests a re-establishment of functional connections between LHA and the spinal cord over time following SCI.

Given the re-establishment of LHA-spinal cord connections during spontaneous recovery after incomplete SCI, we further evaluated whether LHA glutamatergic neurons are necessary for the functional restoration of locomotion. To selectively ablate LHA glutamatergic neurons, we bilaterally injected AAV-DIO-DTR into the LHA of *Vglut2*-Cre mice, followed by DT administration to induce targeted neuronal ablation. After conditional genetic ablation of LHA glutamatergic neurons in hemisection injured mice, we measured basic over-ground locomotion and motivational vigor in fasting-triggered food-seeking behaviors (Fig. 4c). We found that mice with viral-induced depletion of LHA *Vglut2*$^+$ neurons exhibited impaired recovery of locomotor function, as characterized by pronounced paw dragging and impaired protraction of the denervated hindlimb (Fig. 4d–f) (Hindlimb retraction: Two-way RM ANOVA followed by Bonferroni's multiple comparison, 1w $p < 0.0001$, 2w $p < 0.0001$, 4w $p = 0.0006$. Hindlimb protraction: Two-way RM ANOVA followed by Bonferroni's multiple comparison, 1w $p > 0.9999$, 2w $p < 0.0001$, 4w $p = 0.0483$. Height of iliac crest: Two-way RM ANOVA followed by Bonferroni's multiple comparison, 1w $p = 0.8425$, 2w $p > 0.9999$, 4w $p > 0.9999$. Although locomotor function was impaired, general locomotor activity did not significantly differ from that of the controls (Supplementary Fig. 4d) (Center time: $p = 0.6265$, two-tailed, t-test, t = 0.5020, df = 10. Total distance: $p = 0.4188$, two-tailed, t-test, t = 0.8432, df = 10. Entries to center area: $p = 0.8890$, two-tailed, t-test, t = 0.1431, df = 10.). However, in the food seeking test, we observed a significant reduction in both total distance and center entries, indicating the deficit in motivation-driven locomotion rather than generalized motor activity (Fig. 4g and Supplementary Fig. 4e) (1 week after injury: Entries to center area: $p < 0.0001$, two-tailed, t-test, t = 7.447, df = 10. Total distance: $p = 0.0003$, two-tailed, t-test, t = 5.453, df = 10. Number of pellet eaten: $p = 0.5971$, two-tailed, t-test, t = 0.5459, df = 10. 2 weeks after injury: Entries to center area: $p < 0.0001$, two-tailed, t-test, t = 6.936, df = 10. Total distance: $p = 0.0009$, two-tailed, t-test, t = 4.681, df = 10. Number of pellet eaten: $p = 0.7914$, two-tailed, t-test, t = 0.2717, df = 10.).

To specifically deplete PnO-projecting LHA neurons, we injected retrogradely transported AAVs carrying Cre into the PnO while expressing Cre-dependent DTR in the LHA of wild-type mice. This genetic ablation of PnO-projecting LHA neurons also significantly impaired the functional recovery of SCI mice during over-ground locomotion, as evidenced by pronounced paw dragging and impaired protraction of the denervated hindlimb (Fig. 4h–j) (Hindlimb retraction: Two-way RM ANOVA followed by Bonferroni's multiple comparison, 1w $p < 0.0001$, 2w $p < 0.0001$, 4w $p = 0.0406$. Hindlimb protraction: Two-way RM ANOVA followed by Bonferroni's multiple comparison, 1w $p > 0.9999$, 2w $p < 0.0001$, 4w $p = 0.0163$. Height of iliac crest: Two-way RM ANOVA followed by Bonferroni's multiple comparison, 1w $p > 0.9999$, 2w $p > 0.9999$, 4w $p > 0.9999$. No significant difference in general locomotor activity was observed compared with that of controls (Supplementary Fig. 4f) (Center time: $p = 0.8937$, two-tailed, t-test, t = 0.1371, df = 10. Total distance: $p = 0.7823$, two-tailed, t-test, t = 0.2838, df = 10. Entries to center area: $p = 0.7089$, two-tailed, t-test, t = 0.3842, df = 10.). Moreover, impaired functional recovery was associated with decreased food-seeking motivational locomotion after SCI (Fig. 4k and Supplementary Fig. 4g) (1 week after injury: Entries to center area: $p < 0.0001$, two-tailed, t-test, t = 6.713, df = 10. Total distance: $p = 0.0006$, two-tailed, t-test, t = 4.877, df = 10. Number of pellet eaten: $p > 0.9999$, two-tailed, t-test, t = 0.000, df = 10. 2 weeks after injury: Entries to center area: $p = 0.0001$, two-tailed, t-test, t = 6.195, df = 10. Total distance: $p = 0.0003$, two-tailed, t-test, t = 5.414, df = 10. Number of pellet eaten: $p = 0.7137$, two-tailed, t-test, t = 0.3775, df = 10.). These findings suggest that motivational locomotion encoded by PnO-projecting LHA neurons is important for natural repair after incomplete SCI.

Subsequently, we examined the post-injured period in which LHA neuronal activity could exert their action in promoting locomotor recovery. This was achieved by injecting AAVs carrying Cre-dependent ChR2-mCherry into LHA of *Vglut2-Cre* mice prior to SCI, and optogenetically stimulated LHA at 1, 4, and 8 weeks after injury (Fig. 4l). All tested SCI mice demonstrated significantly improved hindlimb locomotion during the period of light stimulation. Detailed kinematic analysis revealed increased weight support and enhanced hindlimb stepping ability (Fig. 4m, n and Supplementary Video 5) (Hindlimb retraction: Two-way RM ANOVA followed by Bonferroni's multiple comparison, 1w $p < 0.0001$, 4w $p < 0.0001$, 8w $p = 0.0006$. Hindlimb protraction: Two-way RM ANOVA followed by Bonferroni's multiple comparison, 1w $p < 0.0001$, 4w $p < 0.0404$, 8w $p = 0.0383$. Height of iliac crest: Two-way RM ANOVA followed by Bonferroni's multiple comparison, 1w $p < 0.0001$, 4w $p = 0.0039$, 8w $p = 0.0065$. These results indicate that LHA neuronal activity results in immediate facilitation of hindlimb motor functions in hemisectioned SCI mice.

Acute LHA stimulation enables stepping in paralyzed mice after stagger SCI

We next investigated whether more clinically relevant DBS at the LHA could improve locomotion in mice with severe SCI. Results described above (Fig. 3b, c) indicated that stimulation of LHA-MSDB pathway induced significant anxiety-like behaviors that are known to be detrimental to recovery[48,49]. Therefore, we aimed to selectively stimulate the LHA-PnO pathway by adjusting the locus of stimulation within the LHA during DBS.

On the basis of the soma distribution of LHA neurons that project to the PnO and MSDB, we identified that the LHA neurons projecting to PnO and MSDB are primarily located in the caudal and rostral region of the LHA (Fig. 3f), respectively. We injected AAVs carrying GCaMP6s into both PnO and MSDB and recorded the activation of these downstream brain regions during electrical stimulation of various locations along the anterior-posterior axis of the LHA (Fig. 5a, b). In head-fixed mice, we found that stimulating the rostral (−1.0 mm from the bregma) and caudal (−1.5 mm from the bregma) LHA resulted in preferential activation of MSDB and PnO, respectively (Fig. 5c–f) (rLHA DBS: Two-way RM ANOVA followed by Bonferroni's multiple comparison, before stimulation $p > 0.9999$, during stimulation $p < 0.0001$. cLHA DBS: Two-way RM ANOVA followed by Bonferroni's multiple comparison, before stimulation $p > 0.9999$, during stimulation $p < 0.0001$. Moreover, electrical stimulation in caudal LHA also induced elevated locomotion immediately in free-moving uninjured mice (Fig. 5g–k) (Total distance: $p < 0.0001$, two-tailed, t-test with Welch's correction, $t = 14.04$, $df = 6.135$. Maximum speed: $p < 0.0001$, two-tailed with Welch's correction, t-test, $t = 13.92$, $df = 5.226$.). These results prompted us to apply DBS at the specific location of LHA to facilitate functional recovery following severe SCI.

We established a staggered SCI model with opposite lateral hemisection at T7 and T10, creating a more challenging scenario by eliminating brain-derived innervation below T10 while maintaining a spared tissue bridge between the two lesions to relay descending signals[17,50]. The mice with this staggered lesion exhibited nearly complete and permanent hindlimb paralysis. The preserved intersegmental relay circuits between the lesions make this model suitable for studying neuromodulation-based recovery strategies. We conducted a time course experiment to assess the effects of LHA-DBS on locomotor function by evaluating animals with and without LHA-DBS at post-injury weeks 1, 4, and 10 and analyzing the immediate effect on hindlimb stepping (Fig. 5l, m). We observed no hindlimb responses to LHA-DBS at 1 week post-injury, but we observed significantly improved walking ability during DBS at 4 weeks post-injury, as indicated by significant increases in maximum iliac crest height and stride length. This DBS effect was observed continuously until at least 10 weeks post-injury (Fig. 5n–p) (Maximum crest height: Two-way RM ANOVA followed by Bonferroni's multiple comparison, 1w $p = 0.2015$, 4w $p = 0.0250$, 10w $p = 0.0013$. Stride length: Two-way RM ANOVA followed by Bonferroni's multiple comparison, 1w $p = 0.2666$, 4w $p = 0.0005$, 10w $p < 0.0001$.

Subsequently, we examined the mechanism by which LHA-DBS facilitates functional improvement in hindlimb locomotion. Previous studies have shown that activation of thoracic long-distance projecting Zfhx3-expressing neurons through spared relay pathways[51,52], such as axonal sprouting of the reticulospinal tract[17,21,22], plays a pivotal role in the restoration of locomotor function following SCI. The mechanisms underlying LHA-DBS are thus likely dependent on the activation of these Zfhx3 neurons. We found that targeted DBS at caudal LHA indeed led to a significant increase in the number of cFos-expressing neurons as well as c-Fos and Zfhx3 co-expressing neurons in the inter-lesion spinal cord at 4 and 10 weeks post-injury, as compared to that observed at 1 week post-injury (Supplementary Fig. 5a–c) ($cFos^+$ $Zfhx3^+/Zfhx3^+$: One-way ANOVA $F(2, 12) = 54.90$ with $p < 0.0001$, followed by Tukey's multiple comparison, 1 week vs 4 weeks $p = 0.0295$, 1 week vs 10 weeks $p < 0.0001$ and 4 weeks vs 10 weeks $p < 0.0001$. Inter-ventral $cFos^+$: One-way ANOVA $F(2, 12) = 51.29$ with $p < 0.0001$, followed by Tukey's multiple comparison, 1 week vs 4 weeks $p = 0.0033$, 1 week vs 10 weeks $p < 0.0001$, and 4 weeks vs 10 weeks $p = 0.0002$. Notably, the behavioral improvement by DBS described above was not maintained after the cessation of stimulation. These findings led to our further investigation of the potential of repetitive long-term LHA-DBS for promoting functional locomotor recovery after SCI.

Intention-gated long-term LHA-DBS enhances locomotor recovery after sever SCI

Previous findings have demonstrated that the delivery of DBS triggers animal's stress-like responses[27,53]. We also observed elevated stress-like response under the condition of LHA-DBS, even for localized caudal LHA stimulation. To reduce this side effect, we applied an intention-gated stimulation algorithm that uses animal's locomotor intention signals to trigger LHA-DBS. We decoded the intention of locomotion with a 32-channel micro-wire array electrode that was implanted in the multi-unit activity (MUA) in the hindlimb region of the motor cortex (M1HL)[27,54] and used the decoded signal to stimulate the LHA via a brain-computer interface (BCI)-DBS system. We found that locomotor intentional signals, as indicated by an increased MUA firing rate prior to the initiation of hindlimb movements, could be observed in both intact and staggered SCI mice (Fig. 6a, b). Furthermore, open-field tests showed that this intention-gated LHA-DBS did not provoke stress-like responses in either healthy or injured mice (Fig. 6c–f) (Intact center time: One-way ANOVA $F(2, 15) = 15.59$ with $p = 0.0002$, followed by Tukey's multiple comparison, control vs DBS $p = 0.0033$, control vs BCI-DBS $p = 0.3623$, and DBS vs BCI-DBS $p = 0.0002$. Intact total distance: One-way ANOVA $F(2, 15) = 8.137$ with $p = 0.004$, followed by Tukey's multiple comparison, control vs DBS $p = 0.0445$, control vs BCI-DBS $p = 0.0034$, and DBS vs BCI-DBS $p = 0.4180$. Intact entries to center area: One-way ANOVA $F(2, 15) = 23.80$ with $p < 0.0001$, followed by Tukey's multiple comparison, control vs DBS $p = 0.0066$, control vs BCI-DBS $p = 0.0134$, and DBS vs BCI-DBS $p < 0.0001$. Stagger injury center time: One-way ANOVA $F(2, 15) = 64.27$ with $p < 0.0001$, followed by Tukey's multiple comparison, control vs DBS $p = 0.5107$, control vs BCI-DBS $p < 0.0001$, and DBS vs BCI-DBS $p < 0.0001$. Stagger injury total distance: One-way ANOVA $F(2, 15) = 38.00$ with $p < 0.0001$, followed by Tukey's multiple comparison, control vs DBS $p < 0.0001$, control vs BCI-DBS $p < 0.0001$, and DBS vs BCI-DBS $p = 0.3611$. Stagger injury entries to center area: One-way ANOVA $F(2, 15) = 53.58$ with $p < 0.0001$, followed by Tukey's multiple comparison, control vs DBS $p = 0.0022$, control vs BCI-DBS $p < 0.0001$, and DBS vs BCI-DBS $p < 0.0001$.

The above findings suggest that an intention-gated BCI-DBS system could be used as a long-term treatment for promoting locomotor recovery after SCI. To test this hypothesis, we apply daily 1-h BCI-DBS treatment sessions to staggered SCI mice for 6 weeks, beginning at 4 weeks post-injury (Fig. 6g). The locomotor function of the mice was assayed by BMS scores weekly at the last day of the treatment without and in the present of DBS. In contrast to the un-treated SCI group, long-term BCI-DBS training resulted in significant functional recovery, including restored hindlimb stepping ability and increased BMS scores without DBS, although DBS during testing could further elevate the motor function (Fig. 6h, i and Supplementary Video 6). Kinematic analysis revealed substantial improvements in locomotion compared with that of the untreated group. For over-ground movement, the mice were able to support their body weight, showed significantly increased hindlimb oscillation, and exhibited muscle activity as confirmed by electromyogram (EMG) recordings (Fig. 6j, k) (Maximal crest height: One-way ANOVA $F(2, 12) = 48.43$ with $p < 0.0001$, followed by Tukey's multiple comparison, control vs training without stim $p = 0.0017$, control vs training with stim $p < 0.0001$ and training without stim vs

https://doi.org/10.1038/s41467-025-67133-5

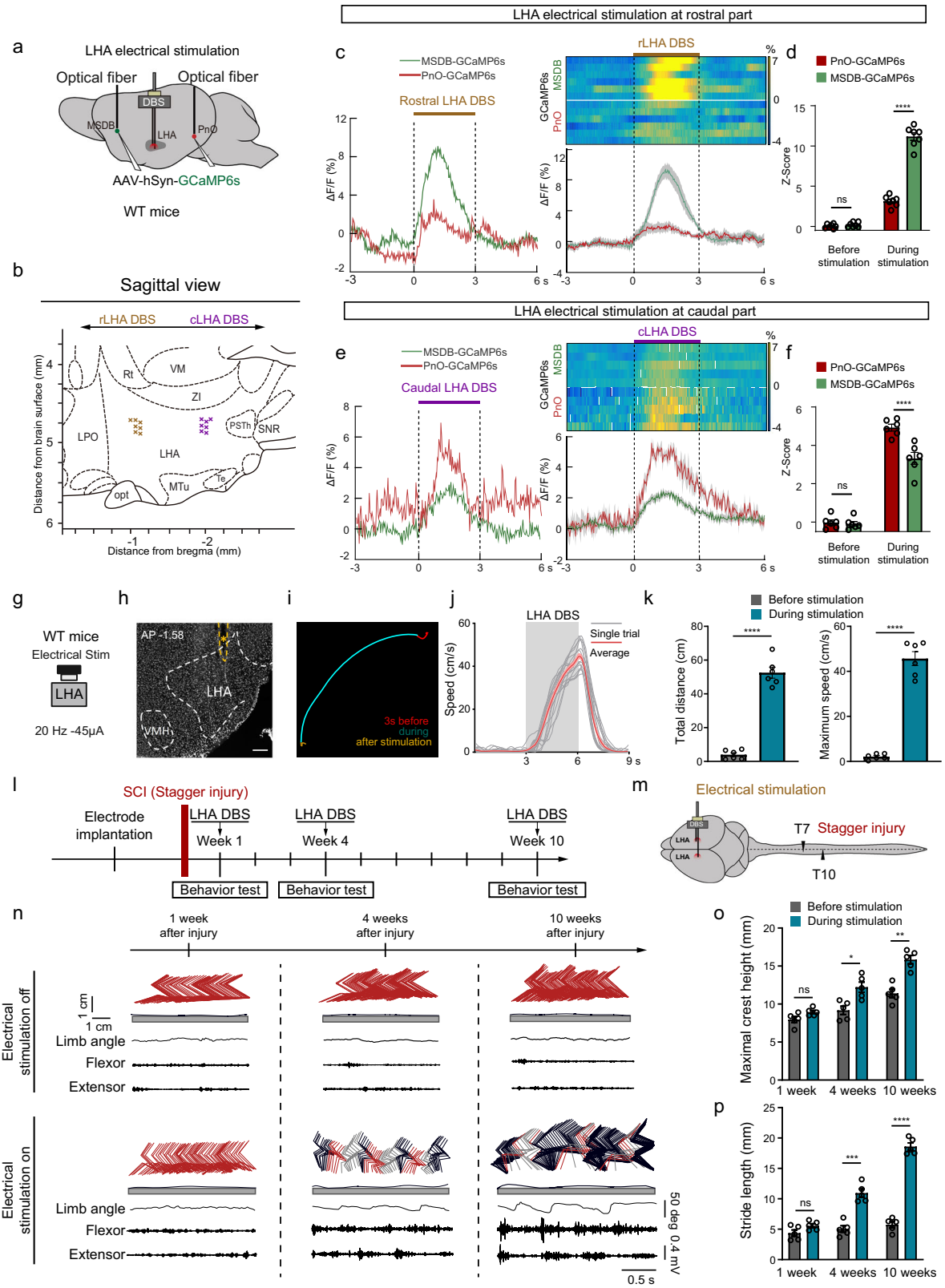

training with stim $p = 0.0005$. Stride length: One-way ANOVA $F(2, 12) = 141.9$ with $p < 0.0001$, followed by Tukey's multiple comparison, control vs training without stim $p = 0.0002$, control vs training with stim $p < 0.0001$, and training without stim vs training with stim $p < 0.0001$. Furthermore, long-term BCI-DBS training led to a significant increase in the number of cFos-positive and cFos/Zfhx3 double-positive neurons in the inter-lesion spinal cord (Supplementary Fig. 6a–c) (cFos$^+$ Zfhx3$^+$/ Zfhx3$^+$: One-way ANOVA $F(2, 12) = 143.5$ with $p < 0.0001$, followed by Tukey's multiple comparison, control vs training without stim $p = 0.0084$, control vs training with stim $p < 0.0001$ and training without stim vs training with stim $p < 0.0001$. Inter-ventral cFos$^+$: One-way ANOVA $F(2, 12) = 66.49$ with $p < 0.0001$, followed by Tukey's multiple comparison, control vs training without stim $p = 0.0044$, control vs training with stim $p < 0.0001$, and training

Fig. 5 | Optimized LHA DBS acutely enables stepping in paralyzed mice after chronic stagger SCI. a Strategy for the simultaneous recording of responses from PnO and MSDB during LHA DBS. **b** Sagittal view of the locus of electrical stimulation at the rostral and caudal part of LHA. The results of electrical stimulation at rostral part of LHA. The calcium signals of an example trial (left) and all trials (right) are shown (**c**). MSDB was predominantly activated when the rostral part of LHA was stimulated (**d**, $n = 6$, $p < 0.0001$). Error bars, SEM. **e**, **f** The results of electrical stimulation at the caudal part of LHA. The calcium signals of an example trial (left) and all trials (right) are shown (**e**). PnO was activated to a greater extent than PnO when the caudal part of LHA was stimulated (f, $n = 6$, $p < 0.0001$). Error bars, SEM. **g** Strategy for electrical stimulation of LHA in intact mice. **h** Coronal view of post-hoc anatomical evaluation of the electrode placement in LHA, in the vicinity of the DBS electrode implantation site. Scale bar, 200 μm. **i** Centre of body mass trajectories of a single trial in open field arena during 3-s time windows: stationary phase (red), electrical stimulation phase (cyan) and after stimulation offset (orange). **j** Speed versus time of single trials (grey lines) and the average (red line) of one mouse. **k** Quantification of total distance (left) and maximum speed (right) of mice before and during electrical stimulation of LHA ($n = 6$). Student's *t*-test (two-tailed, unpaired) was applied. ****$p < 0.0001$. Error bars, SEM. **l**, **m** Timeline and scheme summarizing the experiments. A severe SCI model of staggered lateral hemisections at T7 and T10. **n**–**p** Representative leg kinematics and hindlimb EMG data from SCI mice in the acute injury (7 DPI), and sub-chronic (28DPI) and chronic injury stages (70DPI). Scale bar, 0.4 mV, 0.5 s. Quantification of maximal crest height (**o**) and stride length (**p**) of mice at 1w, 4w and 8 w after stagger injury ($n = 5$). Two-way RM ANOVA followed by Bonferroni's multiple comparison *$p < 0.05$; **$p < 0.01$; ***$p < 0.001$; ****$p < 0.0001$. Error bars, SEM. Source data are provided as a Source data file.

without stim vs training with stim $p < 0.0001$. Collectively, these results indicate that long-term intention-gated LHA-DBS treatment effectively promotes locomotor recovery.

Discussion

The lateral hypothalamus, an evolutionarily conserved brain region, has received significant attention in the studies of emotion, energy metabolism, and innate behaviors. Nonetheless, for innate behaviors involving the spinal cord, its role in normal signaling processing and for therapeutic intervention of behavioral abnormalities such as those leading to obesity and anorexia[55], remains to be elucidated. In this study, we identified a population of glutamatergic neurons in the caudal LHA (cLHA) that transmit excitatory signals to pontine reticulospinal neurons in the PnO, which in turn project to the spinal cord to initiate locomotion. We demonstrated that those PnO-projecting LHA *Vglut2*$^+$ neurons play a crucial role in motivated locomotion during food seeking behavior. Furthermore, the activity of these neurons contributes to various aspects of motor recovery following incomplete spinal cord injury (SCI). Our findings reveal the importance of LHA-PnO pathway in transmitting locomotor commands to the spinal cord, underscore the role of supraspinal circuits in facilitating functional recovery after SCI, and highlight PnO-projecting LHA *Vglut2*$^+$ neurons as promising target for therapeutic interventions.

Pontine reticulospinal projections of cLHA *Vglut2*$^+$ neurons initiate locomotion

Previous studies have shown that stimulation of SLR can induce various motor behaviors. Further electrophysiological mapping showed that stimulation of LHA or its surrounding areas[56,57] within SLR could induce locomotion after ablation of MLR[2,58]. This independence of MLR has led to the notion that SLR plays a specific role in locomotor control. By delivering the PRV virus to the mouse hindlimb muscles, our results revealed an extremely densely labeled region in the caudal LHA. Further studies indicated that activating *Vglut2*$^+$ neurons, but not *Vgat*$^+$ neurons, in this area induced robust mouse locomotion. The widespread projections of the heterogeneous populations of neuronal subtypes within LHA have made deciphering the role of the LHA in locomotor control difficult[33,59]. Recent studies have provided insights into specific neuronal subtypes within the LHA that are involved in regulating movement. For example, *Orexin*-expressing neurons respond to movement on a millisecond timescale[60], and LHA neurons projecting to the PAG[38] or VTA[39] mediate evasion or defensive behavior, respectively. However, the exact pathway by which the LHA regulates locomotion remains to be clarified. We found that the PnO-projecting glutamatergic LHA neurons can reliably induce forward locomotion, and the PnO-SC projections serve as a downstream relay pathway for this behavior. Notably, we also discovered that this LHA-PnO-SC excitatory pathway initiates locomotion without inducing negative emotion, which is thought to be one of the regulatory functions of the LHA.

It remains challenging to fully elucidate the organization of extensive projections of LHA. In this study, we classified the projections of LHA neurons into four major categories on the basis of single-neuron projectome data from fMOST imaging analysis. Notably, we identified a group of LHA neurons projecting to the spinal cord, ~49% of which expressed *Orexin* (Supplementary Fig. 3b). However, activation of these direct spinal cord-projecting LHA neurons did not induce locomotion. In contrast, activation of cLHA neurons projecting to the PnO, including ~21.6% orexin-positive neurons (Supplementary Fig. 3b), robustly initiated locomotion. A previous study has shown that activation of a subpopulation of LHA *Orexin* neurons could initiate locomotion[60]. Our findings further demonstrated that PnO-projecting LHA *Vglut2*$^+$ neurons, a minor population of which also express *Orexin*, are responsible for locomotion initiation. Whether these *Orexin Vglut2*$^+$ neurons play a distinct role in initiating locomotion remains to be examined.

Single-neuron projectome analysis also revealed intriguing projection patterns, including projections with axon collaterals to both PnO and PPN (Supplementary Fig. 3c), which play important roles in exploratory locomotion[5]. However, we found very few neurons projecting to CnF, which is known to be involved in escape behaviors[5].

While the PPN has been widely implicated in locomotor control[5,7,34,43,61], our results revealed that the LHA-PnO pathway can independently drive locomotion without requiring glutamatergic neurons in PPN. This conclusion is directly supported by our experiments demonstrating that optogenetic activation of LHA-PnO projections effectively induces locomotion even when PPN glutamatergic neurons are bilaterally suppressed. Critically, these findings establish the LHA-PnO pathway as a distinct neural substrate for locomotor initiation, functionally distinct from the caudal PPN glutamatergic neuron pathway. Since PPN and CnF are two subregions of MLR, there is potentially a PPN-dependent spinal projecting pathway that is parallel to the LHA-PnO-spinal pathway we identified here. This PPN to spinal cord pathway may also be mediated by PnO, which potentially could transmit a variety of action commands besides motor initiation, such as those for controlling locomotor gait asymmetries and inducing behavioral arrest[44,62]. Given the functional diversity of PnO neurons, further studies are warranted to clarify their distinct roles in various pathways that mediate different aspects of motor behaviors and interactions among various pathways.

LHA circuits in emotional valence processing

The LHA integrates arousal, motivation, and evasion signals[10,63,64] resulting from external challenges and internal drives[39,65], and initiate adaptive behaviors of the animal, including appetitive locomotion[10,66–68]. Our study demonstrated that LHA *Vglut2*$^+$ neurons projecting to the PnO play a crucial role in facilitating motivated locomotion, particularly during goal-directed behaviors such as food-seeking. LHA-PnO ablation caused no significant change in total distance traveled in the open field without food, confirming that the

https://doi.org/10.1038/s41467-025-67133-5

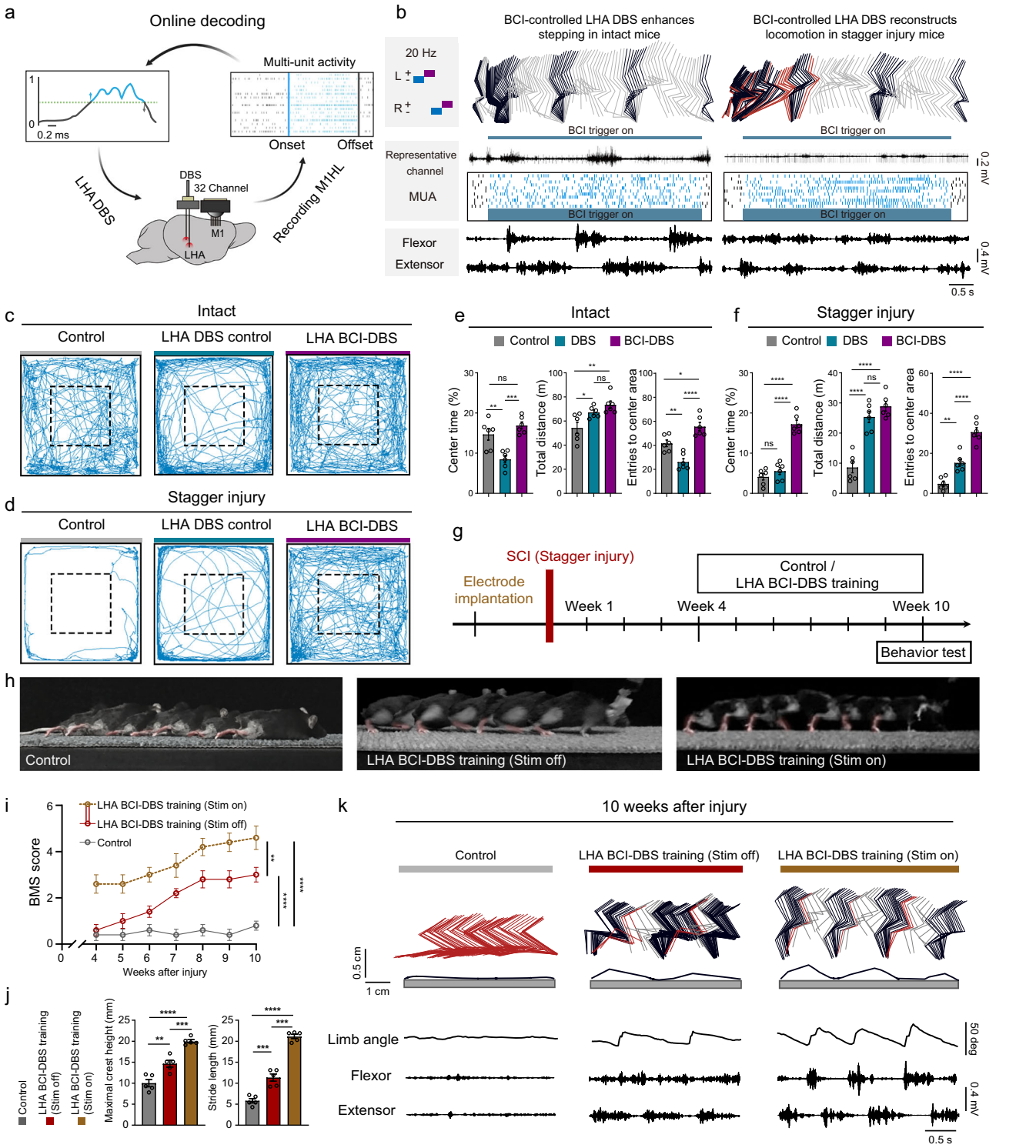

reduced movement that was observed in the food-seeking test was not due to a global motor deficit. The dissociation between locomotor activity in open field and food-seeking contexts strongly indicates that the LHA-PnO circuit specifically modulates motivation-driven locomotion, rather than overall locomotor activity. The context-dependent nature of the behavioral deficits (present with food) supports our conclusion that LHA-PnO circuit is functionally specialized for motivation-driven locomotion. Importantly, locomotion was observed without the induction of anxiety or stress-like behaviors, indicating that the LHA-PnO circuit can selectively enhance motor functions that are associated with motivation without triggering negative emotional states. This finding is particularly interesting because it dissociates the locomotor and emotional functions of the LHA, which has traditionally been closely associated with both motor control and emotional regulation[39].

In addition to the LHA-PnO projection involved in locomotor control, we also identified a distinct LHA-MSDB projection that is involved in evasion and anxiety-like behaviors (Fig. 3a–c). Among the seven subtypes of LHA projection neurons, we categorized based on projection patterns, neurons in the rostral LHA primarily project to subcortical and thalamic areas, such as the lateral septum (LS) and lateral habenula (LHb), suggesting a key role of LHA in emotional

Fig. 6 | Brain-controlled LHA-DBS enhances locomotor recovery after sever SCI. **a** The schematic diagram of LHA DBS triggered by BCI. A 4 * 8 array was used to record neural signals from M1. The multi-unit activity (MUA) was processed online by an unsupervised algorithm. DBS application and intensity depended on the neural activities. **b** Representative leg kinematics, neural activities, and hindlimb EMG data of healthy mice (left) and staggered mice (right). Scale bar of representative neuronal active channel, 0.2 mV. Scale bar of EMG data, 0.4 mV, 0.5 s. **c** Trajectory of intact mice in open-field chambers without DBS (left), with irregular DBS (middle), and with brain-controlled DBS (right). **d** Trajectory of mice after SCI (stagger injury) in open-field chambers without DBS (left), with irregular DBS (middle), and with brain-controlled DBS (right). **e** Quantification of the proportion of center time (left), total distance (middle), and entries to center area (right) in intact mice, comparing no DBS to irregular or brain-controlled DBS ($n = 6$). One-way ANOVA/Tukey's multiple comparison was applied. ns, not significant; $^{*}p < 0.05$; $^{**}p < 0.01$. Error bars, SEM. **f** Quantification of the proportion of center time (left), total distance (middle), and entries to center area (right) in post-SCI (stagger injury) mice, comparing no DBS to irregular or brain-controlled DBS ($n = 6$). One-way ANOVA/Tukey's multiple comparison was applied. ns not significant; $^{****}p < 0.0001$. Error bars, SEM. **g** Timeline summarizing the experiments about the effect of LHA brain-controlled DBS in the recovery process of mice following stagger SCI. **h** Chronophotography of mice illustrates the recovery process following a stagger injury. **i** BMS test performance in control, BCI-DBS training without stimulation, and BCI-DBS training with stimulation groups. $n = 5$ per group, two-way ANOVA-RM with Bonferroni post hoc correction. $^{**}p < 0.01$, $^{****}p < 0.0001$. Error bars, SEM. **j** Quantification of maximal crest height (left) and stride length (right) of mice at 70 DPI without training, trained without DBS, or trained with DBS ($n = 5$). One-way ANOVA/Tukey's multiple comparison was applied. $^{**}p < 0.01$; $^{***}p < 0.001$; $^{***}p < 0.0001$. Error bars, SEM. **k** Representative leg kinematics and hindlimb EMG data from mice without training (left), trained without stimulation (middle), and trained with stimulation (right) after stagger injury. Source data are provided as a Source data file.

regulation, consistent with past findings[53,69]. We found that activation of LHA *Vglut2*$^{+}$ neurons projecting to the MSDB induced anxiety-like behaviors, suggesting their role in emotional responses to potential threats. This finding was further confirmed by the finding that stimulation of LHA *Vglut2*$^{+}$ neurons terminals in MSDB resulted in escape-like high-speed movements. The role of LHA-MSDB projection in mediating anxiety and evasion aligns is in line with previous findings of MSDB's involvement in modulating emotional states, particularly those related to fear and anxiety[70,71]. The involvement of this circuit in both anxiety and escape-like behaviors suggests that it plays a critical role in coordinating negative emotion and motor responses[41,70,72].

The dissociation between the LHA-PnO and LHA-MSDB pathways in terms of locomotion initiation vs. anxiety-like motor behaviors suggests that different subsets of LHA *Vglut2*$^{+}$ neurons are functionally segregated, with some circuits promoting motivated actions and others modulating emotion-related behaviors. This dissociation suggests that activation of selective LHA neurons involved in motor control could promote locomotion in intact and SCI mice without exacerbating negative emotional states, such as anxiety or depression[53]. This is particularly important in the context of SCI treatment, where emotional disturbances often hinder the rehabilitation efforts to motor recovery[49].

Therapeutic potential of DBS and its implications for clinical translation in SCI

By elucidating the circuit mechanism underlying LHA's control of locomotion, we have provided the circuit basis for the application of DBS in promoting functional recovery after SCI. Our findings show that DBS stimulation of LHA, particularly targeting its glutamatergic neurons, significantly improved locomotor function in SCI mice. Guided by viral tracing and single-neuron projectome analysis, we identified the optimal stimulation locus in LHA that provides more selective activation of the LHA-PnO-spinal pathway. This selective activation facilitated the restoration of locomotor function in SCI mice without inducing stress. To maximize the efficacy of DBS, we further developed a brain-controlled DBS system that leverages real-time decoding of motor cortex activity to restrict the timing and duration of LHA stimulation in line with the mouse's intention to walk. This intention-gated system was shown to minimize the stress-like behaviors induced by prolonged DBS, facilitate the immediate initiation of motor action, and promote long-term restoration of hindlimb motor function. By applying LHA stimulation concurrently with the animal's motor intention, which should intrinsically activate appropriate motor initiation circuits that likely include LHA-PnO-spinal pathway, DBS action effectively amplify the intrinsic activation of latter motor initiation pathway. Under the condition of SCI, such concurrent DBS stimulation (within ~10 ms following M1 signials) could potentiate the synaptic efficacy of residue functional LHA-PnO-spinal circuit or promote the formation of compensatory propriospinal circuits for motor recovery. This intention-gated DBS for targeting selectively motor initiation circuit allows for a more precise and personalized approach for motor rehabilitation.

Moreover, our findings raise important questions regarding the potential advantages of LHA-DBS compared to stimulation of other locomotor-related structures, such as the MLR, which consists of the CnF and PPN. Compared with traditional DBS targets in the CnF and PPN, LHA stimulation demonstrates several notable neurobiological and clinical advantages. Most significantly, LHA targeting achieves robust motor improvements while substantially reducing the risk of stimulation-induced adverse effects, particularly stress and anxiety. Furthermore, LHA stimulation appears to elicit more generalized motivational effects that synergistically enhance both volitional gait initiation and adaptive locomotor control, whereas CnF/PPN stimulation tends to produce more stereotypic stepping patterns.

Limitations of this study

There are several limitations of the present study. First, although we demonstrated that LHA stimulation enhances locomotor recovery in mice, the efficacy of LHA-DBS in more clinically relevant models has not been explored. For example, SCI models of non-human primates may exhibit injury and recovery conditions that more closely resemble to those of SCI patients. Second, we did not fully characterize the side effects of LHA-DBS on eating behaviors, which are known to be regulated by LHA. Although we found optogenetic stimulation of LHA inhibitory neurons had no effect on mouse locomotion, whether this stimulation also causes disorders in feeding behaviors was not examined. Finally, we did not fully address more complex issues of human spinal cord injuries, a wider range of injury patterns, comorbidities, and recovery over long duration. is unknown. Such side effects of LHA-DBS are important issues to address for clinical application of LHA-DBS.

In conclusion, our study identified the LHA as a brain region that is critical for initiating locomotion and motor recovery following spinal cord injury (SCI). By modulating the activity of the pontine reticulospinal pathway, LHA excitatory neuron activity enhances motivated locomotion without triggering stress responses. Our results indicate selective activation of LHA-PnO-spinal pathway could be an effective therapeutic treatment for SCI. Additionally, our development of motor cortical activity-gated DBS system offers a more effective and safer intention-gated approach of DBS treatment for SCI.

Methods

Mouse strains

The following mouse lines were used in this study: wild-type C57BL/6 (SLAC Laboratory Animal, Shanghai), *Vglut2*-ires-Cre mice (The Jackson Laboratory, Stock 016963), *Vgat*-ires-Cre mice (The Jackson

Laboratory, Stock 016962). Eight-to twelve-week-old male and female mice were randomly assigned to experimental groups. All mice were housed under consistent conditions with unrestricted access to food and water and maintained on a 12-h light/dark cycle (lights on from 7:00 a.m. to 7:00 p.m.). Before food seeking test, mice were fasted for 24 h. All animal studies and experimental procedures received approval from the Animal Care and Use Committee of the Institute of Neuroscience, Chinese Academy of Sciences.

Retrograde trans-synaptic PRV tracing

In the retrograde trans-synaptic tracing experiments, mice were anesthetized with intraperitoneal injection of Zoletil 50 (30 mg/kg) in combination with Xylazine Hydrochloride (40 mg/kg) and placed on the surgical table. An incision was made on the left to expose the tibialis anterior muscle. Three injection sites were made at a depth of 0.5–1.0 mm into the muscle through the microliter syringes (Hamilton). At each site, 1 μL PRG-EGFP (Braincase) was injected. Following the PRV injection, the incision was sutured. For histological analysis, mice were perfused at 5.5 days after the PRV injection.

Transparency and 3D image acquisition

All harvested samples were post-fixed overnight at 4 °C in 4% PFA in PBS. The solution of Benzyl Alcohol and Benzyl Benzoate (BABB) was then used to match the refractive index of the tissue. Cleared samples were imaged in a transverse orientation on a light-sheet microscope. The samples were scanned using the continuous light-sheet scanning method with the included contrast blending algorithm for the 564 nm channels. Cell detection was performed with the newly developed open-source ClearMap software[73], tailored for cell nuclei, which used a background subtraction via morphological opening, followed by a sequence of filters, morphological operations, and a 3D peak detection. The color of the bubble corresponds to n^2 fold change in cell density in HY.

Stereotactic surgery

Stereotactic injections into both the brain and spinal cord were performed using a microinjection syringe pump (World Precision Instruments, WPI) and a stereotactic apparatus (RWD Life Science). Prior to surgery, mice were anesthetized by intraperitoneal injection of Zoletil 50 (30 mg/kg) in combination with Xylazine Hydrochloride (40 mg/kg).

For the stereotactic injections into the brain, the skull of the head-immobilized mouse was exposed and treated with 3% hydrogen peroxide to remove connective tissue from the surface. The skull was then leveled anteroposteriorly between the bregma and lambda, and mediolaterally between the left and right hemispheres. A small hole was drilled in the skull at the precise coordinates corresponding to the target brain region. Virus was delivered to the target brain region at a rate of 50 nL/min using the microinjection syringe pump (WPI). When the injection was completed, the micropipette was held in place for 10 min, then raised up by 0.1 mm following an additional 3 min, and finally withdrawn at a low speed.

The coordinates for different brainstem targets are as follows (zero from Bregma; AP, anterior-posterior; ML, medial-lateral; DV, dorsal-ventral from dura; in mm): LHA, AP -1.58, ML ± 1.0, DV 4.95; PnO, AP -4.3, ML ± 0.85, DV 3.95; MSDB, AP + 1.00, ML ± 0.10, DV 3.60; M1, AP -0.7 to -1.2, ML ± 1.0, DV 0.55; Gi, AP -6.0, ML ± 0.35, DV 5.10; SNr, AP -3.2, ML ± 1.15, DV 4.30; LPGi, AP -6.90, ML ± 1.10, DV 5.00; MLR, AP -4.80, ML ± 1.19, DV 2.70; LDT, AP -5.20, ML ± 0.70, DV 2.50; PCG, AP -5.50, ML ± 0.40, DV 3.1; LHA rostral part, AP -1.06, ML ± 1.0, DV 4.95; LHA caudal part, AP -2.00, ML ± 1.0, DV 4.95.

To implant an optical fiber in the target brain region for optical stimulation or fiber photometry recording, we drilled 3 to 4 small holes into the surface of the skull and inserted skull screws. Simultaneously, we polished the surface of skull with a cranial drill to increase friction. After drilling the hole at the coordinates corresponding to the target brain region, the optical fiber was slowly lowered into the brain using the stereotactic arm at a speed of 1 mm/min. Once the optical fiber was in place, the gap in the skull was first filled with a biocompatible adhesive, and this was followed by primary fixation with light-curing adhesive, and finally the optical fiber was secured to the skull with dental cement.

To retrogradely target supraspinal neurons, we injected viruses into the lumbar segment of spinal cord. For the stereotactic injection into the spinal cord, a dorsal incision was made along the spine at the level of the lumbar segment. The overlying muscles were stripped to expose the lumbar spine, and a laminectomy was performed to expose the spinal cord. The virus was injected into the lumbar spinal cord at a rate of 60 nL/min. After the injection, the micropipette was held in place for a few minutes before it was slowly withdrawn.

Viral vectors in experiments

For optogenetic activation of LHA in Figs. 1 and 4 and Supplementary Figs. 1 and 4, AAV2/9-EF1α-DIO-ChR2-mCherry (BrianVTA; 5.6×10^{12}) was injected into the LHA. For fiber photometry experiments in Figs. 1, 5 and Supplementary Fig. 1, AAV2/9-hSyn-DIO-GCaMP6s (BrianCase; 6.7×10^{12}) was injected into the LHA. For deletion of LHA in Figs. 1 and 4, AAV2/9-EF1α-DIO-DTR-mCherry (BrianVTA; 6.0×10^{12}) was injected into the LHA. For retrograde anatomical tracing experiments in Figs. 2 and 3, AAV2/2Retro-EF1α-DIO- ChR2-EYFP (BrianCase; 5.7×10^{12}) was injected into the spinal cord. For optogenetic activation of LHA-PnO or MSDB pathway in *Vglut2*-Cre mice in Fig. 2, AAV2/2Retro-EF1α-DIO-FLP (BrianVTA; 4.7×10^{12}) was injected into PnO or MSDB, and AAV2/9-hSyn-fDIO-ChR2-mCherry (BrianVTA; 5.0×10^{12}) was injected into the LHA. For optogenetic activation of LHA-PnO or MSDB pathway in WT mice in Supplementary Fig. 2, AAV2/2Retro-EF1α-Cre (BrianVTA; 5.4×10^{12}) was injected into PnO or MSDB, and AAV2/9-EF1α-DIO-ChR2-mCherry (BrianVTA; 5.6×10^{12}) was injected into the LHA. For chemogenetic inhibition of the PPN in Supplementary Fig. 2, AAV2/9-EF1α-DIO-hM4Di-EGFP (BrianCase; 6.4×10^{12}) was bilaterally injected into the PPN. For deletion of LHA-PnO or MSDB pathway in Fig. 3, AAV2/2Retro-EF1α-Cre (BrianVTA; 5.4×10^{12}) was injected into PnO or MSDB, AAV2/9-EF1α-DIO-DTR-mCherry (BrianVTA; 6.0×10^{12}) was injected into the LHA. For anterograde anatomical tracing experiments in Fig. 3, AAV2/9-EF1α-DIO-ChR2-mCherry (BrianVTA; 5.6×10^{12}) was injected into the PnO. For optogenetic activation of PnO neurons receiving LHA projection in Fig. 3, AAV2/1-hSyn-Cre (BrianVTA; 1.4×10^{13}) was injected into the LHA, and AAV2/9-EF1α-DIO-ChR2-mCherry (BrianVTA; 5.6×10^{12}) was injected into the PnO. For optogenetic activation of PnO-spinal cord in Supplementary Fig. 3, AAV2/2Retro-EF1α-DIO-ChR2-EYFP (BrianCase; 4.2×10^{12}) was injected into the spinal cord. For anatomical tracing of LHA-PnO-spinal cord pathway in Fig. 3, AAV2/2Retro-EF1α-Cre (BrianVTA; 5.4×10^{12}) was injected into the spinal cord, AAV2/8-EF1α-DIO-H2B-EGFP-T2A-TVA (BrianVTA; 5.2×10^{12}) and AAV2/8-EF1α-DIO-RVG (BrianVTA; 4.2×10^{12}) were injected into the PnO, and RV-EvnA-DsRed (BrianVTA; 2.1×10^{8}) was injected into the PnO. For optogenetic activation of LHA-PnO-spinal cord pathway in Fig. 3, AAV2/1-hSyn-FLP (BrianVTA; 1.5×10^{13}) was injected into the LHA, and AAV2/2Retro-EF1α-ConFon-ChR2-mCherry (BrianCase; 4.0×10^{12}) was injected into the spinal cord. For deletion of LHA-PnO or MSDB in Fig. 4 and Supplementary Fig. 4, AAV2/2Retro-EF1α-Cre (BrianVTA; 5.4×10^{12}) was injected into PnO or MSDB, AAV2/9-EF1α-DIO-DTR-mCherry (BrianVTA; 6.0×10^{12}) was injected into the LHA.

Optogenetic manipulation

Each optic fiber was attached to a 473 nm laser device (Shanghai Laser & Optics Century Co., Ltd, ADR 700 A), and the laser pulses were triggered and stopped by a custom-written MATLAB code. For general optogenetic activation, a blue light stimulation with 473 nm a

frequency of 10 Hz, and pulse duration of 40 ms was used. Laser power settings were adjusted for each mouse and maintained throughout all experiments. The power of the laser was between 10 and 40 mW at the connector. In the runway test, we recorded locomotion 3 s before stimulation, during the 3-s light pulse, and 3 s post-stimulation. For open field, elevated plus maze test, and food seeking test, each trial consisted of a 10-s light stimulation followed by a 20-s no-light interval.

Single-neuron projectome: data acquisition and analysis

Sparse labeling strategy. To achieve sparse and cell type-specific neuronal labeling across distinct neuropeptidergic populations, we employed a combination of conditional viral strategies in Cre-driver mouse lines targeting Adcyap1, Nts, Tac1, Tac2, Penk, Pdyn, SST, Oxytocin, MCH, Trh, CRH, and Orexin. Sparse labeling was accomplished either by injecting low-titer Cre-dependent AAVs expressing GFP variants or co-injecting Cre-dependent FlpO-expressing AAVs with FlpO-dependent fluorescent reporter AAVs at specific ratios. Additionally, for direct Orexin neuron labeling, we delivered AAVs encoding mNeoGreen under the control of the Orexin promoter (PPORX) into wild-type males. Together, these methods allowed us to achieve sparse labeling of multiple neuropeptide-defined neuronal subtypes with high specificity[40].

fMOST imaging and preprocessing. As outlined in previous descriptions, the fMOST imaging process was carried out. Initially, the brains that had been dissected were subjected to post-fixation in 4% paraformaldehyde (PFA) before being embedded in Lowicryl HM20 resin (Electron Microscopy Sciences, 14340). Subsequently, the brains were imaged in a propidium iodide (PI) filled water bath using an fMOST microscope, achieving a voxel resolution of 0.32 × 0.32 × 1 μm. The surface of the sample in a coronal plane was then imaged to trace the neurons (GFP) and register the brain (PI channels), after which it was sectioned in 1 μm increments using a fixed diamond knife. This procedure, involving cycles of sectioning and imaging, was repeated until comprehensive imaging of the entire brain sample was accomplished.

We used a proprietary software tool, Fast Neurite Trace (FNT), to specifically trace long-range axon projections in the datasets produced by light microscopy. Initially, the software's "slice2cube" function divides the original image data into more manageable 3D data cubes. At any given moment, approximately eight adjacent cubes around a specified position are automatically loaded into the computer's memory and rendered in 3D for tracing. The tracing process consists of identifying a potential path, scrutinizing it, and expanding the existing neurite tree. User confirmation is required at each step to ensure the accuracy of the tracing process. This method allows for the comprehensive tracing of an axon projection. To ensure quality control, different neurons within the same sample were traced by different team members concurrently, with results cross-validated upon completion. Moreover, each traced neuron underwent an independent review by a separate individual to confirm accuracy. Additionally, we conducted random post-tracing quality checks on each brain sample.

The entire brain, complete with the information of all reconstructed neurons, was registered into the standard Allen CCFv3 using a method previously described. To summarize, we segmented several brain regions as landmarks, using cytoarchitecture references. We then executed a diffeomorphic transformation and symmetric image normalization using Advanced Normalization Tools (ANTs). This process enabled us to acquire transformation parameters based on these landmarks. Subsequently, these transformation parameters were applied to all the traced neurons within the brain sample. This allowed us to remap the reconstructed neuron onto the Allen brain template. The neurons with caudal projections that extend beyond the standard brain are thought to project to the spinal cord cervical c1 segment.

Neuron exclusion. We carried out manual checks on all neurons to confirm the accuracy of the tracing. Neurons that been found to have incorrect tracing data and with soma locations outside the lateral hypothalamus were excluded from subsequent analysis, after which a total of 916 neurons located in the LHA were incorporated in our analysis. All the neurons were mirrored to the same hemisphere prior to analysis.

Parameter calculation and neuron visualization. Utilizing the standard Allen CCFv3 annotation file as a reference, we computed the soma location, axon length, and terminal number for each neuron in every brain region. This was achieved using a Python library we developed, which is available at https://pypi.org/project/pyswcloader/. All neuron visualizations were generated using a self-developed Python package, neuron-vis (https://gitee.com/bigduduwxf/neuron-vis).

Hierarchical clustering of LHA neurons based on axon morphology. The projections and morphological information of LHA reconstructed neurons can be downloaded from our publicly accessible website (https://mouse.digital-brain.cn/projectome/lha).

To obtain the similarity matrix of axon morphology, first, we extracted the coordinates of each point from the original morphological file of each neuron, which were referred to by neuron P and Q, respectively. For each point i in the neuron P, we calculated the shortest distance to neuron Q and denoted this value as d(Pi→Q). The same calculation was performed on each point j of neuron Q to obtain the shortest distance to neuron P, which is denoted by d(Qj→P). Then we calculated a parameter α, the proportion of data points smaller than the mean value in each set of shortest distance, to get the weighted average value according to the value in each set of shortest distance, to get the weighted average value according to the following formula:

$$d(P \to Q) = \alpha * \mathrm{mean}(d(Pi \to Q)) + (1-\alpha) * \max(d(Pi \to Q))$$

$$d(Q \to P) = \alpha * \mathrm{mean}(d(Qj \to P)) + (1-\alpha) * \max(d(Qj \to P))$$

The similarity score between neuron P and Q was calculated as the mean value of d(P → Q) and d(Q → P). Then, hierarchical clustering using Ward's linkage was performed on the similarity score matrix to identify the subtypes. The neurons projecting to the cervical spinal cord were assigned a fixed value.

DTR-mediated cell ablation. For local inhibition of the LHA, we injected Cre-dependent AAVs carrying diphtheria toxin receptor (DTR) into LHA of the *Vglut2-Cre* mice. For intersectional inhibition of PnO or MSDB projecting LHA neurons, we first injected AAV2-retro-Cre into the PnO or MSDB and then injected AAV-DIO-DTR-mCherry into the LHA of wild type mice. Three weeks after DTR injection, diphtheria toxin (DT, 50 μg/kg, Sigma) was intraperitoneally injected for three consecutive days to deplete the neurons. All the behavioral tests were conducted at least seven days after the DT injection. To confirm the effects of neuronal lesions, mice were sacrificed and perfused.

Chemogenetic experiments. Following at least 2 weeks for the expression of hM4Di, 2 mg/kg Clozapine N-oxide (CNO, BrainVTA) was injected intraperitoneally 1 h before behavioral tests. Prior to experiments, all animals received daily handling for 2 weeks to reduce stress-induced confounding factors associated with manual manipulation and injection procedures.

Optical-fiber-based Ca2+ recording in freely behaving mice. After 3 weeks of surgery, fiber photometry recording was carried out by using a commercial device (RWD Life Science, Shenzhen, China) as previously described. In brief, laser beams of 470 nm and 410 nm were initially launched into the fluorescence cube, then launched into the optical fibers. The 410 nm laser was used for motion control. The

emission fluorescence from both the GCaMP and control was collected by a camera at the frequency of 20 Hz. The in vivo recordings were carried out within a custom-made open field box (40 × 40 × 40 cm), with food placed in a corner.

We calculated the value of the photometry signal, denoted as F, using the ratio F_{470}/F_{410}. We then computed ΔF/F as $(F - F_0) / F_0$, where F_0 is the median of the photometry signal. Only behaviors with calcium signals exceeding 3 standard deviations (SD) were treated as events. The average of 10 peak ΔF/F and the number of events per minute for each mouse were analyzed.

Single unit recording and analysis. The 32-channel drivable electrodes were hand-assembled as previously described[74]. Custom tetrode arrays were manually fabricated, with 8-channel tetrodes mounted on a microdrive. Each tetrode was formed by twisting 13-μm polyimide-coated wires, and their tips were gold-plated to reduce impedance, resulting in a final impedance range of 500–800 kΩ (measured at 1 kHz). The tips of the tetrodes were implanted above the LHA and the electrodes were then fixed to the skull with dental cement. Recordings began five days after surgery, during which mice were allowed to move freely in a linear runway (1.5 m long × 15 cm wide × 20 cm high). After each recording, the electrodes were advanced by 100–200 μm. All signals were acquired using TDT system (Tucker-Davis Technologies, USA), digitalized and sampled at 24 kHz, then bandpass filtered online (0.7–3 kHz). The stored data was converted and then processed using Offline Sorter for single-cell isolation (Plexon, Inc., TX, USA). The corresponding speed was obtained from synchronized videos recorded by the TDT system, which were analyzed using EthoVision XT (Noldus). The correlation between firing rate and speed was analyzed in a manner similar to previous work[7].

EMG recording. For electromyography (EMG) recording, we performed implantation of customized bipolar electrodes into selected hindlimb muscles to record EMG activity. Electrodes (793200, A-M Systems) were guided by 30-gauge needles and inserted into the mid-belly of the medial gastrocnemius (GS) and tibialis anterior (TA) muscles of the hindlimb. A common ground wire was inserted subcutaneously in the neck-shoulder area. Wires were routed subcutaneously through the back to a small percutaneous connector, which was securely cemented to the skull of the mouse. EMG signals were acquired using a TDT system (RA32 pre-amplifier + RZ2 base processor) controlled by Synapse software (TDT) with a filtration range of 10–1000 Hz. The acquired signals were analyzed using custom-written MATLAB scripts.

Behavioral experiments and kinematic analysis. Motor functions were assessed weekly with a locomotor open field rating scale, the Basso Mouse Scale (BMS)[75]. All BMS behavioral tests were conducted by investigators who were blinded to the treatment groups.

Behavioral tracking of mouse movements was performed offline utilizing DeepLabCut (https://github.com/DeepLabCut/). Behavioral tests included overground locomotion of mice either prior to or throughout the recovery period following SCI on an elevated runway. More than 15% of the frames were selected from the behavioral videos of mice in different states to serve as the initial training datasets. To quantify the gait characteristics of mice before and after SCI, frames in the training datasets were manually labeled for the iliac crest, hip, knee, ankle, and toe. A ResNet-50 network was trained for 1×10^5 iterations on the initial training datasets, and the network with the lowest loss value was selected for subsequent analysis through evaluation. Videos representative of different mice were analyzed using the trained ResNet-50 network to obtain the labeled videos and the coordinates of the labeled points.

Kinematic variables were computed using custom scripts in MATLAB (v.R2018a, MathWorks), based on the x, y coordinates generated by DeepLabCut. The whole limb oscillation was evaluated by calculating the angle of the virtual limb linking hip to toe. The speed of toe was calculated by taking one frame from every six frames to determine whether the mouse was in the stance or swing phase, with the threshold being adjusted for each individual mouse. To visualize the movement of mice, we extracted a 3-s segment from the videos of different mice and displayed the labeled points and skeleton lines of their lower limbs.

Open-field (OF) test food seeking test and elevated plus maze (EPM). The test apparatus consisted of a rectangular box (40 × 40 × 30 cm). A dim light was applied above the field. Before the experiment, the mouse was put into the test room for a 30-min acclimation period. Subsequently, the mouse was gently placed into the center of the rectangular box for free exploration. The time spent in the center zone (20 × 20 cm), as well as the total distance and center time traveled in the whole open field arena, were measured over 20 min. For assessing the effect of BCI on reducing anxiety-like behavior in animals, animals in the BCI group triggered LHA-DBS using M1 signals. The control group was tested by providing stimulus pulses equivalent to the median number of pulses that trigger stimulation in the BCI group, with these stimulus pulses being applied either at regular intervals or randomly.

Specifically, for the group assigned to the task of food seeking, mice underwent a 24-h food restriction period prior to the test to enhance their motivation to food seeking during the assessment. During the fasting and testing period, they were maintained at more than 90% of their free-feeding body weight. Food pellets were placed in the center area and could be obtained by a single mouse in the open field for 20 min.

The EPM (Elevated Plus-Maze) apparatus used in our study consisted of a central region (5 × 5 cm), two open arms (30 × 5 cm), and two enclosed arms (30 × 5 × 15 cm). The apparatus, arranged in a "+" configuration, was situated 50 cm above the floor. At the beginning of the EPM test, the mice were placed in the central area, oriented towards an enclosed arm, and allowed to explore for a duration of 10 min.

In addition, we utilized EthoVision XT (Noldus) and custom-written MATLAB scripts to extract the total time that the animals spent in each zone of the open field or each arm of the EPM. Example trajectories were generated using EthoVision XT (Noldus). For both the open field and EPM test, we calculated the velocity by dividing the total distance by the moving time, data for which was also extracted using EthoVision XT.

SCI surgical procedures. The procedure for the T7 and T10 double lateral hemisection and T10 lateral hemisection was performed by a surgical technician. For the T7 and T10 double lateral hemisection, a T7-T10 laminectomy was made over the thoracic vertebrae. We utilized a scalpel and micro-scissors to disrupt the bilateral dorsal columns to make the T7 right-side over-hemisection, to make sure no sparing of the ventral pathways on the contralateral side. We carefully sectioned only the left side of the spinal cord up to the midline at T10. Subsequently, the muscle layers were sutured, and the skin was secured using wound clips. For the T10 lateral hemisection, a midline incision was made over the thoracic vertebrae followed by a T10 laminectomy. The unilateral hemisection was then performed carefully using both scalpel and micro-scissors, avoiding, to the greatest extent, the damage of the spinal cord dura.

Post-surgical treatments and care of the animals. Following SCI in adult mice, we administered a subcutaneous injection of 1 mL saline, positioned food on the floor of their cages, and ensured that they were kept warm until they regained consciousness. We undertook manual bladder emptying procedures twice a day and monitored for signs of

dehydration and any clinical indicators of pain or infection. In case of a urinary infection, we initiated a course of antibiotherapy (Baytril, 10 mg/kg, for 5 days). Any mice exhibiting a body weight reduction exceeding 15% were humanely euthanized.

Deep brain stimulation. The deep brain stimulation (DBS) apparatus is composed of bipolar parallel tungsten wires, each with a diameter of 0.1 mm and a length of 5.5 mm. The insulation was removed at a length of 200 µm from the tip. The two electrodes were spaced 2.2 mm apart to bilaterally target the LHA. The DBS electrodes were secured to the head with dental cement. The mice were allowed to recover in their home cages for at least 3 days before starting the behavioral tests.

In the electrical stimulation mapping experiments, a stimulating electrode was lowered into the LHA under ketamine anesthesia. The electric current of −75 µA, 0.5 µs was delivered at a frequency of 45 Hz for 5 s, with intervals of 30–60 s between trials. The peak-to-peak amplitude and latency of the evoked responses were analyzed from EMG recordings of the right tibialis anterior (TA) muscle. Evaluations were conducted both with and without stimulation. The selected stimulation sites were strategically positioned along the AP axis of LHA at the coordinates of −0.54, −1.04, −1.54, −2.04, and −2.54 mm.

Intention-gated DBS. Two electrodes for recording and LHA stimulation were implanted under aseptic conditions and general anesthesia. To record the activities of M1 neurons, a 32-channel microelectrode array (4 × 8 array of tungsten wires, spaced 100 µm apart) was inserted into layer V of the hindlimb area of the primary motor cortex (M1). In addition, a deep brain stimulation (DBS) apparatus was inserted in the LHA. The ground and reference wires from the array were attached to screws fixed to the skull.

During online testing, neural signals from M1 were monitored in real-time. Whenever the value of y = wn exceeded a detection threshold within the range of 0.7–0.8, the real-time processor administered LHA-DBS. Conversely, the DBS was halted when it fell to the threshold within the range of 0.2–0.3[27].

Immunohistochemistry and Imaging. Mice were perfused with phosphate-buffered saline (PBS) followed by 4% paraformaldenhyde (PFA) in PBS. The brain and spinal cord were removed and postfixed in 4% PFA at 4 °C for 24 h. The tissue was dehydrated in 30% sucrose solution at 4 °C for 24 h and sectioned coronally into 40 µm slices with a Cryostat microtome (Thermo Scientific HM525 NX). The sections were washed with PBS (6 * 10 min) and then blocked with a blocking solution (PBS containing 10% donkey serum and 4% Triton X-100) at room temperature for 2 h. Then the sections were incubated with the primary antibodies at 4 °C for 24 h. Upon completion of the primary antibody incubation, the sections were washed with PBS (6 * 10 min) and then incubated with secondary antibodies at room temperature for 2 h. After the 2-h incubation, the sections were thoroughly washed with PBS (6 * 10 min) and mounted with anti-fade mounting medium with DAPI for imaging. Sections were photographed using the Olympus VS120 virtual slide system.

Quantification and statistical analysis. All analyses were conducted blindly with respect to experimental conditions, using GraphPad Prism 10.0 software or MATLAB (v2018a). A two-tailed Student's *t*-test was employed for single comparisons between two groups. For all other data, one-way or two-way ANOVA was utilized based on the appropriate experimental design. Post hoc analyses were performed exclusively when a main effect reached statistical significance, with *P* values for multiple comparisons adjusted using Bonferroni's correction. All data are presented as the mean ± SD unless otherwise stated. ns, not significant; $p > 0.05$; $^{*}p < 0.05$; $^{**}p < 0.01$; $^{***}p < 0.001$; $^{****}p < 0.0001$. Mice were randomized by litter, body weight, and sex before assignment to treatment groups; no additional specific randomization was implemented for the animal studies.

Reporting summary

Further information on research design is available in the Nature Portfolio Reporting Summary linked to this article.

Data availability

Source data are provided with this paper. All datasets required to reproduce the figures are included. Any further requests can be addressed to the corresponding authors (Y.L. and W.C.). Source data are provided with this paper.

Code availability

The code supporting this study has been deposited in a publicly accessible GitHub repository: GitHub Repository: https://github.com/Lilab2025/Single-neuron-projectome-of-Lateral-Hypothalamus.

References

1. Arber, S. & Costa, R. M. Connecting neuronal circuits for movement. *Science* **360**, 1403–1404 (2018).
2. Shik, M. L. & Orlovsky, G. N. Neurophysiology of locomotor automatism. *Physiol. Rev.* **56**, 465–501 (1976).
3. Sinnamon, H. M. Preoptic and hypothalamic neurons and the initiation of locomotion in the anesthetized rat. *Prog. Neurobiol.* **41**, 323–344 (1993).
4. Kiehn, O. Decoding the organization of spinal circuits that control locomotion. *Nat. Rev. Neurosci.* **17**, 224–238 (2016).
5. Caggiano, V. et al. Midbrain circuits that set locomotor speed and gait selection. *Nature* **553**, 455–460 (2018).
6. Capelli, P., Pivetta, C., Soledad Esposito, M. & Arber, S. Locomotor speed control circuits in the caudal brainstem. *Nature* **551**, 373–377 (2017).
7. Roseberry, T. K. et al. Cell-type-specific control of brainstem locomotor circuits by basal Ganglia. *Cell* **164**, 526–537 (2016).
8. Ferreira-Pinto, M. J. et al. Functional diversity for body actions in the mesencephalic locomotor region. *Cell* **184**, 4564–4578 e4518 (2021).
9. Stuber, G. D. Neurocircuits for motivation. *Science* **382**, 394–398 (2023).
10. Saper, C. B. & Lowell, B. B. The hypothalamus. *Curr. Biol.* **24**, R1111–R1116 (2014).
11. Ferreira-Pinto, M. J., Ruder, L., Capelli, P. & Arber, S. Connecting circuits for supraspinal control of locomotion. *Neuron* **100**, 361–374 (2018).
12. Gao, L. et al. Single-neuron projectome of mouse prefrontal cortex. *Nat. Neurosci.* **25**, 515–529 (2022).
13. Qiu, S. et al. Whole-brain spatial organization of hippocampal single-neuron projectomes. *Science* **383**, eadj9198 (2024).
14. Gao, L. et al. Single-neuron analysis of dendrites and axons reveals the network organization in mouse prefrontal cortex. *Nat. Neurosci.* **26**, 1111–1126 (2023).
15. Li, H. et al. Single-neuron projectomes of mouse paraventricular hypothalamic nucleus oxytocin neurons reveal mutually exclusive projection patterns. *Neuron* **112**, 1081–1099.e1087 (2024).
16. Winter, C. C. et al. A transcriptomic taxonomy of mouse brain-wide spinal projecting neurons. *Nature* **624**, 403–414 (2023).
17. Chen, B. et al. Reactivation of dormant relay pathways in injured spinal cord by KCC2 manipulations. *Cell* **174**, 521–535.e513 (2018).
18. Anderson, M. A. et al. Natural and targeted circuit reorganization after spinal cord injury. *Nat. Neurosci.* **25**, 1584–1596 (2022).
19. Asboth, L. et al. Cortico-reticulo-spinal circuit reorganization enables functional recovery after severe spinal cord contusion. *Nat. Neurosci.* **21**, 576–588 (2018).

20. Sawada, M. et al. Function of the nucleus accumbens in motor control during recovery after spinal cord injury. *Science* **350**, 98–101 (2015).
21. Takeoka, A., Vollenweider, I., Courtine, G. & Arber, S. Muscle spindle feedback directs locomotor recovery and circuit reorganization after spinal cord injury. *Cell* **159**, 1626–1639 (2014).
22. Zörner, B. et al. Chasing central nervous system plasticity: the brainstem's contribution to locomotor recovery in rats with spinal cord injury. *Brain J. Neurol.* **137**, 1716–1732 (2014).
23. Masini, D. & Kiehn, O. Targeted activation of midbrain neurons restores locomotor function in mouse models of Parkinsonism. *Nat. Commun.* **13**, 504 (2022).
24. Hofer, A. S. et al. Stimulation of the cuneiform nucleus enables training and boosts recovery after spinal cord injury. *Brain Neurol.* **145**, 3681–3697 (2022).
25. Roussel, M., Lafrance-Zoubga, D., Josset, N., Lemieux, M. & Bretzner, F. Functional contribution of mesencephalic locomotor region nuclei to locomotor recovery after spinal cord injury. *Cell Rep. Med.* **4**, 100946 (2023).
26. Bachmann, L. C. et al. Deep brain stimulation of the midbrain locomotor region improves paretic hindlimb function after spinal cord injury in rats. *Sci. Transl. Med.* **5**, 208ra146 (2013).
27. Bonizzato, M. et al. Multi-pronged neuromodulation intervention engages the residual motor circuitry to facilitate walking in a rat model of spinal cord injury. *Nat. Commun.* **12**, 1925 (2021).
28. Burnside, E. R. & Bradke, F. Mesencephalic locomotor region stimulation-cuneiform or pedunculopontine? *Cell Rep. Med.* **4**, 100948 (2023).
29. Stieglitz, L. H. et al. Deep brain stimulation for locomotion in incomplete human spinal cord injury (DBS-SCI): protocol of a prospective one-armed multi-centre study. *BMJ Open* **11**, e047670 (2021).
30. Cho, N. et al. Hypothalamic deep brain stimulation augments walking after spinal cord injury. *Nat. Med.* **30**, 3676–3686 (2024).
31. Kirst, C. et al. Mapping the fine-scale organization and plasticity of the brain vasculature. *Cell* **180**, 780–795.e725 (2020).
32. Renier, N. et al. Mapping of brain activity by automated volume analysis of immediate early genes. *Cell* **165**, 1789–1802 (2016).
33. Wang, Y. et al. EASI-FISH for thick tissue defines lateral hypothalamus spatio-molecular organization. *Cell* **184**, 6361–6377.e6324 (2021).
34. Carvalho, M. M. et al. A brainstem locomotor circuit drives the activity of speed cells in the medial entorhinal cortex. *Cell Rep.* **32**, 108123 (2020).
35. Zhou, T. et al. History of winning remodels thalamo-PFC circuit to reinforce social dominance. *Science* **357**, 162–168 (2017).
36. Buzsáki, G., Leung, L. W. & Vanderwolf, C. H. Cellular bases of hippocampal EEG in the behaving rat. *Brain Res.* **287**, 139–171 (1983).
37. Tang, Y., Benusiglio, D., Grinevich, V. & Lin, L. Distinct types of feeding related neurons in mouse hypothalamus. *Front. Behav. Neurosci.* **10**, 91 (2016).
38. Li, Y. et al. Hypothalamic circuits for predation and evasion. *Neuron* **97**, 911–924.e915 (2018).
39. Barbano, M. F. et al. VTA glutamatergic neurons mediate innate defensive behaviors. *Neuron* **107**, 368–382.e368 (2020).
40. Jiao, Z. et al. Projectome-based characterization of hypothalamic peptidergic neurons in male mice. *Nat. Neurosci.* **28**, 1073–1088 (2025).
41. Fuhrmann, F. et al. Locomotion, theta oscillations, and the speed-correlated firing of hippocampal neurons are controlled by a medial septal glutamatergic circuit. *Neuron* **86**, 1253–1264 (2015).
42. Sinnamon, H. M. & Stopford, C. K. Locomotion elicited by lateral hypothalamic stimulation in the anesthetized rat does not require the dorsal midbrain. *Brain Res.* **402**, 78–86 (1987).
43. Krauth, N., Sach, L. K., Sitzia, G., Clemmensen, C. & Kiehn, O. A hypothalamus-brainstem circuit governs the prioritization of safety over essential needs. *Nat. Neurosci.* **28**, 1473–1485 (2025).
44. Cregg, J. M., Sidhu, S. K., Leiras, R. & Kiehn, O. Basal ganglia-spinal cord pathway that commands locomotor gait asymmetries in mice. *Nat. Neurosci.* **27**, 716–727 (2024).
45. Zhang, G. W. et al. Medial preoptic area antagonistically mediates stress-induced anxiety and parental behavior. *Nat. Neurosci.* **24**, 516–528 (2021).
46. Zingg, B. et al. AAV-mediated anterograde transsynaptic tagging: mapping corticocollicular input-defined neural pathways for defense behaviors. *Neuron* **93**, 33–47 (2017).
47. Liu, Y. et al. A sensitized IGF1 treatment restores corticospinal axon-dependent functions. *Neuron* **95**, 817–833 e814 (2017).
48. Fukutoku, T. et al. Sex-related differences in anxiety and functional recovery after spinal cord injury in mice. *J. Neurotrauma* **37**, 2235–2243 (2020).
49. Ditunno, J. F. Jr. & Formal, C. S. Chronic spinal cord injury. *N. Engl. J. Med.* **330**, 550–556 (1994).
50. Beauparlant, J. et al. Undirected compensatory plasticity contributes to neuronal dysfunction after severe spinal cord injury. *Brain J. Neurol.* **136**, 3347–3361 (2013).
51. Osseward, P. J. et al. Conserved genetic signatures parcellate cardinal spinal neuron classes into local and projection subsets. *Science* **372**, 385–393 (2021).
52. Squair, J. W. et al. Recovery of walking after paralysis by regenerating characterized neurons to their natural target region. *Science* **381**, 1338–1345 (2023).
53. Zheng, Z. et al. Hypothalamus-habenula potentiation encodes chronic stress experience and drives depression onset. *Neuron* **110**, 1400–1415.e1406 (2022).
54. Mirfathollahi, A., Ghodrati, M. T., Shalchyan, V. & Daliri, M. R. Decoding locomotion speed and slope from local field potentials of rat motor cortex. *Comput. Methods Prog. Biomed.* **223**, 106961 (2022).
55. Hsu, T. I. et al. Effectiveness of deep brain stimulation in treatment of anorexia nervosa and obesity: a systematic review. *World Neurosurg.* **168**, 179–189 (2022).
56. Farrell, J. S. et al. Supramammillary regulation of locomotion and hippocampal activity. *Science* **374**, 1492–1496 (2021).
57. Li, Z., Rizzi, G. & Tan, K. R. Zona incerta subpopulations differentially encode and modulate anxiety. *Sci. Adv.* **7**, eabf6709 (2021).
58. Mori, S. Integration of posture and locomotion in acute decerebrate cats and in awake, freely moving cats. *Prog. Neurobiol.* **28**, 161–195 (1987).
59. Mickelsen, L. E. et al. Single-cell transcriptomic analysis of the lateral hypothalamic area reveals molecularly distinct populations of inhibitory and excitatory neurons. *Nat. Neurosci.* **22**, 642–656 (2019).
60. Karnani, M. M. et al. Role of spontaneous and sensory orexin network dynamics in rapid locomotion initiation. *Prog. Neurobiol.* **187**, 101771 (2020).
61. Josset, N. et al. Distinct contributions of mesencephalic locomotor region nuclei to locomotor control in the freely behaving mouse. *Curr. Biol.* **28**, 884–901.e883 (2018).
62. Giber, K. et al. A subcortical inhibitory signal for behavioral arrest in the thalamus. *Nat. Neurosci.* **18**, 562–568 (2015).
63. de Araujo Salgado, I. et al. Toggling between food-seeking and self-preservation behaviors via hypothalamic response networks. *Neuron* **111**, 2899–2917.e2896 (2023).
64. Tye, K. M. Neural circuit motifs in valence processing. *Neuron* **100**, 436–452 (2018).
65. Viskaitis, P. et al. Orexin neurons track temporal features of blood glucose in behaving mice. *Nat. Neurosci.* **27**, 1299–1308 (2024).

66. Harris, G. C., Wimmer, M. & Aston-Jones, G. A role for lateral hypothalamic orexin neurons in reward seeking. *Nature* **437**, 556–559 (2005).
67. Mahler, S. V., Moorman, D. E., Smith, R. J., James, M. H. & Aston-Jones, G. Motivational activation: a unifying hypothesis of orexin/hypocretin function. *Nat. Neurosci.* **17**, 1298–1303 (2014).
68. Jordan, L. M. Initiation of locomotion in mammals. *Ann. N. Y. Acad. Sci.* **860**, 83–93 (1998).
69. Stamatakis, A. M. et al. Lateral hypothalamic area glutamatergic neurons and their projections to the lateral habenula regulate feeding and reward. *J. Neurosci.* **36**, 302–311 (2016).
70. Zhang, G. W. et al. Transforming sensory cues into aversive emotion via septal-habenular pathway. *Neuron* **99**, 1016–1028 e1015 (2018).
71. Li, X. et al. Molecularly defined and functionally distinct cholinergic subnetworks. *Neuron* **110**, 3774–3788.e3777 (2022).
72. Justus, D. et al. Glutamatergic synaptic integration of locomotion speed via septoentorhinal projections. *Nat. Neurosci.* **20**, 16–19 (2016).
73. Renier, N. et al. iDISCO: a simple, rapid method to immunolabel large tissue samples for volume imaging. *Cell* **159**, 896–910 (2014).
74. Lin, L. et al. Large-scale neural ensemble recording in the brains of freely behaving mice. *J. Neurosci. Methods* **155**, 28–38 (2006).
75. Basso, D. M. et al. Basso Mouse Scale for locomotion detects differences in recovery after spinal cord injury in five common mouse strains. *J. Neurotrauma* **23**, 635–659 (2006).

Acknowledgements

We thank Drs Mu-ming Poo, Zhigang He, Philip Williams, Yang Xiang and Bo Chen for critically reading the manuscript. We thank the CEBSIT Mouse Brain Mesoscopic Connectome Core Facility for their assistance in data analysis and the Gene Editing Core Facility for their assistance in virus technology services. This work was supported by the National Natural Science Foundation of China (92168105 and 82461160319 to Y. Li, 82372394 to W. Cai, 82272499 to J. Fan, 82301563 to Z. Li, 82401616 to S. Yu, 82272715 to J. Chen and 82301488 to Z. Zheng), National Science and Technology Major Project of the Ministry of Science and Technology of China (No. 2025ZD0215101 to J. Fan) and Biosecurity Research Project (23SWAQ24 to Y. Li and J. Chen). Y. Li acknowledges the support from Shanghai Municipal Science and Technology Major Project (2018SHZDZX05). W. Cai acknowledges the support from Major Basic Research Fund of Jiangsu Province Hospital (TS202402).

Author contributions

Y.L. and W.C. pioneered and designed the project. C.J., Y.Z., Z. Lin., Z. Zhao., Z.J., Z. Zheng., Z. Li., S.Y., Y.Q., Y.W., A.S., H.S., R.T., and Q.W. performed the experiments and discussed the results. X.Y., X.X., J.C., B.C., W.C., X.W., B.Z. T.X. J.F., and X.S. participated in data analysis, Y.L., C.J., Y.Z., and Z. Lin. prepared the manuscript with input from all authors and all authors were involved in interpretation of experiments and contributed to writing the paper.

Competing interests

The authors declare no competing interests.

Additional information

Supplementary information The online version contains supplementary material available at https://doi.org/10.1038/s41467-025-67133-5.

Correspondence and requests for materials should be addressed to Weihua Cai or Yi Li.

Peer review information *Nature Communications* thanks Roberto Leiras and the other anonymous reviewer(s) for their contribution to the peer review of this work. A peer review file is available.